# FIGNL1 AAA+ ATPase remodels RAD51 and DMC1 filaments in meiotic DNA replication and recombination

**Masaru Ito[1]*, Asako Furukohri[1], Kenichiro Matsuzaki[1, 2], Yurika Fujita[1], Atsushi Toyoda[3], and Akira Shinohara[1]***

[1]Institute for Protein Research, Osaka University, Suita, Osaka 565-0871, Japan
[2]Department of Advanced Bioscience, Graduate School of Agriculture, Kindai University, Nara city, Nara 631-8505, Japan
[3]Advanced Genomics Center, National Institute of Genetics, Mishima, Shizuoka 411-8540, Japan

Running title: FIGNL1 in mouse meiosis

Keywords: meiosis; homologous recombination; FIGNL1; RAD51; DMC1

*Corresponding author:
Masaru Ito; msrito2@protein.osaka-u.ac.jp
Akira Shinohara; ashino@protein.osaka-u.ac.jp

Lead contact:
Akira Shinohara
Institute for Protein Research, Osaka University,
3-2 Yamadaoka, Suita, Osaka 565-0871 JAPAN
Phone: 81-6-6879-8624
FAX: 81-6-6879-8626
E-mail: ashino@protein.osaka-u.ac.jp
ORCID: 0000-0003-4207-8247

**Summary**

The formation of RAD51/DMC1 filaments on single-stranded (ss)DNAs, which is essential for homology search and strand exchange in DNA double-strand break (DSB) repair and for the protection of stalled DNA replication forks, is tightly regulated in time and space. FIGNL1 AAA+++ ATPase plays positive and negative roles in the RAD51-mediated recombination in human cells. However, the role of FIGNL1 in gametogenesis remains unsolved. Here, we characterized a germ-line-specific conditional knockout (cKO) mouse of *FIGNL1*. The *Fignl1* cKO male mice showed defective chromosome synapsis and impaired meiotic DSB repair with the accumulation of RAD51/DMC1 on chromosomes in mid-meiotic prophase I, supporting a role of FIGNL1 in a post-assembly stage of RAD51/DMC1 filaments. *Fignl1* cKO spermatocytes accumulate RAD51 and DMC1 ensembles on chromosomes not only in early meiotic prophase I but also in meiotic S-phase. These RAD51/DMC1 assemblies are independent of meiotic DSB formation. Finally, we showed that purified FIGNL1 dismantles RAD51 filament on double-stranded (ds)DNA as well as ssDNA. These results suggest a critical role of FIGNL1 to limit the uncontrolled assembly of RAD51 and DMC1 on native dsDNAs during the meiotic S-phase and meiotic prophase I.

## Introduction

RAD51 is a central player in homologous recombination in eukaryotes by catalyzing homology-directed repair such as the repair of DNA double-strand breaks (DSBs) in both somatic and meiotic cells. RAD51 also plays a role in S-phase for the protection of stalled DNA replication forks [1, 2], which is independent of RAD51-mediated strand exchange [3, 4]. Moreover, RAD51 is important for the protection of chromosome ends such as telomeres by promoting the incorporation of Telomeric repeat-containing RNA (TERRA) into telomeres for the formation of a unique telomere DNA structure [5]. RAD51-mediated DNA transactions are critical in the maintenance of genome stability, thus suppressing tumorigenesis.

As an active form for homology search and strand exchange, multiple protomers of RAD51 bind to single-stranded (ss)DNAs in the presence of ATP to form a right-handed helical filament termed RAD51 nucleofilament, in which ssDNAs are extended 1.5-2.0-fold relative to the B-form DNA [6-9]. RAD51 nucleofilament is highly dynamic; its assembly and disassembly are controlled by multiple proteins/complexes. The RAD51 mediator promotes the assembly of RAD51 nucleofilament on the ssDNAs coated with an ssDNA-binding protein, RPA (Replication protein A), which hampers RAD51 binding to the ssDNA. The RAD51 mediator in humans includes BRCA2(-PALB2-DSS1) [10], BRCA1-BARD1 [11], RAD52 [12-14], SWI5-SFR1/MEI5 [15, 16], and five RAD51 paralogs (RAD51B, -C, -D, XRCC2, and -3) in vertebrates including humans. The RAD51 paralogs form two distinct complexes: RAD51C-XRCC3 and RAD51B-RAD51C-RAD51D-XRCC2 [17]. SWSAP1 is a distinct member of a RAD51 paralog [18-20], which forms a complex with SWS1 and SPIDR. In addition to its role in RAD51 assembly, the SWI5-SFR1/MEI5 stabilizes RAD51 filament by suppressing ATP hydrolysis by RAD51 [16, 19, 21]. At the post-assembly stage, RAD51 nucleofilament works together with the SWI2/SNF2 family, RAD54 and RAD54B [22, 23], and RAD51AP1 [24-26] for efficient homology search and strand exchange with a target double-stranded DNA (dsDNA) for the formation of displacement (D)-loop. RAD51-mediated strand invasion provides a template for DNA synthesis for further processing of the intermediates for the completion of the repair.

The dynamics of the RAD51 filament are also negatively regulated by proteins that disassemble the filament. Various DNA helicases are involved in the disassembly of RAD51 filament, which include BLM [27-29], FANCJ [30], RECQ5 [31, 32], and FBH1 [33, 34] as well as a degenerate DNA helicase, PARI [35]. RADX is an

86 ssDNA binding protein that modulates RAD51 filament assembly [36, 37]. RAD51-
87 mediated invasion intermediates are also remodeled by other DNA helicases
88 such as WRN, RTEL1, FANCM, and RECQ1 [38]. The stabilization and
89 destabilization of RAD51 filaments are associated with the choice of a
90 homologous recombination pathway. The disruption of RAD51 filaments and/or
91 the D-loop leads to the synthesis-dependent strand annealing pathway (SDSA)
92 for non-crossover formation [39]. On the other hand, stabilization of DNA
93 intermediates such as D-loop facilitates the formation of an intermediate with
94 Holliday structure, whose resolution leads to both crossover (CO) and non-
95 crossover (NCO) recombinants.
96 Meiosis is a specialized cell division that produces haploid gametes.
97 Homologous recombination, specifically crossing-over, is essential for
98 chromosome segregation of homologous chromosomes during meiosis I. To
99 ensure the crossover formation in meiosis, highly programmed regulation is
100 implanted on the recombination pathway [40-42]. A meiosis-specific RAD51 cousin,
101 DMC1, confers the uniqueness on homology search in meiotic recombination [43].
102 The cooperation of RAD51 and DMC1 promotes homology search between
103 homologous chromosomes rather than sister chromatids whose mechanism is
104 one big enigma in the field [44, 45]. RAD51/DMC1-mediated recombination requires
105 meiosis-specific proteins as well as proteins playing a role in somatic cells.
106 Knockout (KO) of the most of genes necessary for homologous recombination,
107 *Rad51* and RAD51 mediators (*Brca2*, *Rad51B*, *-C*, *-D*, *Xrcc2*, and *-3*), in mice
108 leads to embryonic lethality [46-52]. *Swsap1* (and *Sws1* and *Spidr*) KO mice are
109 viable but are sterile [18, 53]. Indeed, SWSAP1-SWS1-SPIDR is necessary for the
110 efficient formation of RAD51/DMC1 focus, which is a cytologically detectable
111 immuno-stained structure, in male meiosis [18, 53, 54]. Moreover, a meiosis-specific
112 HSF2BP(MEILB2)-BRME1(MEIOK21) complex promotes the assembly of
113 RAD51/DMC1 working together with BRCA2 mainly in male meiotic
114 recombination [55-58]. Like RAD51 mediators, KO mice of some negative regulators
115 such as BLM are also embryonically lethal [59] while *Rad54* KO mice are viable
116 and fertile [60].
117 A recently identified recombination regulator, FIGNL1, encodes an AAA+
118 ATPase which belongs to microtubule severing proteins including Katanin,
119 Spastin, and Fidgetin with an N-terminal microtubule-binding domain [61]. FIGNL1
120 was identified as a RAD51-interacting protein and is required for homologous
121 recombination in human somatic cells [62]. FIGNL1 knockdown does not affect

122 DSB-induced RAD51 focus formation [53, 62], suggesting its role in the post-RAD51
123 assembly step. In addition to its positive role in RAD51 assembly, FIGNL1 also
124 functions as a negative regulator for homologous recombination. FIGNL1
125 depletion rescues defective RAD51-focus formation in human cells depleted for
126 SWSAP1 or SWS1, but not for RAD51C [53]. Moreover, purified FIGNL1 promotes
127 the dissociation of RAD51 protein from ssDNAs, which is suppressed by
128 SWSAP1 [53]. In *Arabidopsis thaliana* meiosis, a mutant of *FIGL1*, FIGNL1 ortholog,
129 as well as its partner, *FLIP*, shows increased frequencies of COs during meiosis,
130 indicating a role as an anti-CO factor [63, 64]. The role of FIGL1-FLIP as the anti-CO
131 factor is also seen in rice meiosis [65, 66]. Importantly, the *figl1* mutation can
132 suppress defective RAD51/DMC1 focus formation in *brca2* mutant meiocytes,
133 indicating antagonism of FIGL with the RAD51 mediator [67]. These suggest that
134 RAD51 mediators might play a distinct function in different recombination
135 pathways. Although FIGNL1 plays a role in homologous recombination by
136 regulating the SWSAP1 complex in somatic cells [53], it remains unknown how
137 FIGNL1 regulates recombination and works together with SWSAP1 during
138 meiosis.
139 In this study, we analyzed the role of FIGNL1 in mice, particularly in male
140 meiosis. *Fignl1* KO mice show embryonic lethality, indicating that FIGNL1 plays
141 an essential role in early embryonic development. To explore the role of FIGNL1
142 in meiosis, we constructed a germ-cell specific conditional knockout (cKO) mouse
143 and found that *Fignl1* depletion in the testis led to defective spermatogenesis.
144 Meiotic chromosome spreads from *Fignl1* cKO spermatocytes showed a two-fold
145 increase in the numbers of RAD51 and DMC1 foci relative to controls, suggesting
146 the role of FIGNL1 in the post-assembly stage of not only RAD51 filament but
147 also DMC1 filament. This defective disassembly results in the defective loading
148 of proteins necessary for crossover formation. We also found that FIGNL1
149 suppresses RAD51 and DMC1 assembly in meiotic S-phase and early leptonema,
150 which are independent of meiotic DSB formation. This is supported by the
151 formation of RAD51 and DMC1 foci in spermatocytes from *Spo11* null mice
152 defective in meiotic DSB formation. Moreover, *Fignl1* cKO ameliorates defective
153 RAD51- and DMC1-focus formation in KO spermatocytes of *Swasp1,* a
154 RAD51/DMC1 mediator, supporting the antagonistic role of FIGNL1 to SWSAP1
155 in the assembly of not only RAD51 but also DMC1. Together, our study
156 establishes a dual role of FIGNL1 in mammalian male meiosis. The same
157 conclusion was obtained by Baudat's group by characterizing the *Fignl1* cKO as

158 well as *Flip* cKO (FLIP is a FIGNL1-interacting protein, accompanying paper).
159
160 **Results**
161 ***Fignl1* is essential for early mouse embryogenesis**
162 To determine the functions of FIGNL1 in mice, we created a conditional allele of
163 *Fignl1* gene, *Fignl1*$^{flox}$, in which the exon 3 encoding an open reading frame of
164 the full-length protein is flanked by the *loxP* sites (Fig. 1a) in C57BL/6 background.
165 A null allele of the gene, *Fignl1*$^{\Delta}$, was obtained by breeding with *CAG-Cre*+ mice
166 that constitutively express Cre recombinase. *Fignl1*$^{\Delta/+}$ heterozygous mice grew
167 normally and did not show any apparent defects. Breeding between male and
168 female of *Fignl1*$^{\Delta/+}$ produced *Fignl1*$^{+/+}$ and *Fignl1*$^{\Delta/+}$ pups, but no *Fignl1*$^{\Delta/\Delta}$
169 homozygous pups (0/186 from 38 litters), showing that *Fignl1*$^{\Delta/\Delta}$ mice are not
170 viable. This is consistent with the reported lethality of *Fignl1* knockout (KO) mice
171 in the International Mouse Phenotyping Consortium (IMPC)
172 (https://www.mousephenotype.org). In a detailed analysis of different embryonic
173 stages by the breeding of heterozygous parents, we could not obtain *Fignl1*$^{\Delta/\Delta}$
174 homozygous embryo at both E7.5 and E13.5 stages (0/29 and 0/37, respectively),
175 showing very early lethality of mice homozygous for *Fignl1* deletion. Early
176 embryonic lethality in mice homozygous for the homologous recombination
177 genes has been reported; *Rad51* [52], *Brca2*, [68] and Rad51 paralogs (*Rad51B*, *-C*,
178 *-D*, *Xrcc2*, and *-3*) [46-51].
179
180 ***Fignl1* conditional knockout mice are defective in spermatogenesis**
181 To know the role of FIGNL1 in male meiosis, we generated *Fignl1*$^{flox/\Delta}$ mice
182 harboring a germ-line specific Cre recombinase gene, *Stra8-Cre*. The *Stra8-Cre*
183 gene ensured the expression of Cre not only in spermatocytes (meiotic cells) but
184 also in spermatogonia (mitotic stem cells) [69]. *Fignl1*$^{flox/\Delta}$ *Stra8-Cre*$^{+}$*,* hereafter
185 *Fignl1* conditional knockout *(*cKO), male mice were characterized for
186 spermatogenesis. *Fignl1* cKO adult male mice showed normal body weight
187 without any morphological defects but reduced sizes of the testis by ~50%
188 relative to controls (*Fignl1*$^{+/+}$*, Fignl1*$^{flox/\Delta}$*,* and *Fignl1*$^{+/+}$ *Stra8-Cre*$^{+}$), which is a
189 characteristic of mutants with defective spermatogenesis (Fig. 1b, c). The
190 western blotting analysis confirmed decreased amounts of FIGNL1 protein in the
191 whole testis extracts (Fig. 1d). The level of residual FIGNL1 protein is consistent
192 with the efficiency of Stra8-Cre-mediated excision of *Fignl1*$^{flox}$ allele estimated by
193 the transmission of *Fignl1*$^{\Delta}$ allele from *Fignl1*$^{flox/+}$ *Stra8-Cre*$^{+}$ male mice (91.3%;

194 116/127). Sperm count showed a ~6-fold reduction in its number; residual sperms
195 might come from *Fignl1*$^{flox/\Delta}$ cells where Stra8-Cre recombinase failed excision of
196 the *Fignl1*$^{\Delta}$ allele (Fig. 1e). Histological analysis showed that seminiferous
197 tubules in *Fignl1* cKO testes contained decreased numbers of late spermatocytes
198 and spermatids (Fig. 1f). These indicate a critical role of FIGNL1 in
199 spermatogenesis.
200 To analyze meiotic defects in *Fignl1* cKO male mice, we prepared surface-
201 spread chromosomes of spermatocytes and immuno-stained for meiosis-specific
202 chromosomal proteins, SYCP3(Scp3) and SYCP1(Scp1), which are components
203 of lateral/axial elements and central region of the synaptonemal complex (SC),
204 respectively [70-72]. In leptonema of control spermatocytes, SYCP3 shows thin-line
205 staining structures that indicate elongating chromosome axes (from short to long
206 lines). In zygonema, regions of two thin chromosome axes are paired locally to
207 form a thick line of SYCP3, where SYCP1 proteins are deposited for the assembly
208 of the SC central region. From early zygonema to early pachynema, SC
209 elongates along entire chromosomes, resulting in pachytene chromosome
210 configuration with 19 fully paired thick SYCP3 lines colocalized with SYCP1 and
211 partially paired X-Y bivalent. In *Fignl1* cKO spermatocytes, like in controls,
212 SYCP3-positive lines were formed in leptonema and short lines of SYCP1 in
213 zygonema were also observed. However, there were fewer pachytene and
214 diplotene cells in *Fignl1* cKO relative to controls (22.6±2.4% and 11.4±6.2%
215 compared to 44.7±11.0% and 24.3±7.7%, respectively; Fig. 1g). We also
216 evaluated the expression of FIGNL1 protein in testicular cell squashes by
217 categorizing SYCP3-positive meiotic cells into two: cells before pachynema (i.e.
218 leptonema and zygonema) with a pan-nuclear γH2AX staining and those after
219 pachynema (i.e. pachynema and diplonema) with a large γH2AX staining on the
220 X-Y pair (the sex body) [73] (Extended Data Fig. 1). In controls, cells both before
221 and after pachynema were 100% positive for FIGNL1 staining. In contrast, while
222 only ~25% of cells prior to pachynema were positive for FIGNL1, cells after
223 pachynema were nearly 100% positive in *Fignl1* cKO (Fig. 1h). This indicates that
224 *Fignl1*$^{\Delta/\Delta}$ cells are depleted at either late zygonema or early pachynema from
225 *Fignl1* cKO testes. Further analysis of surface-spread chromosomes revealed
226 abnormal SC formation such as synapsis between non-homologous
227 chromosomes (67.7±2.0% of cells compared to 13.6±4.1% in controls) and
228 multivalent synapsis (26.8±10.9 % of cells compared to 3.1±2.7% in controls) in
229 *Fignl1* cKO (Fig. 1i, j), which could be defined as “pachytene-like” stage as seen

230 in other meiotic recombination defective mutants such as *Dmc1* and *Meiob* KO,
231 etc. [74-76]. These results show that FIGNL1 is necessary for full synapsis of meiotic
232 chromosomes in late zygonema and/or early pachynema and that most of the
233 FIGNL1-depleted cells seem to die at these stages or do not progress further.
234
235 **FIGNL1 promotes the disassembly of DMC1 in male meiosis**
236 To know the effect of *Fignl1* cKO on meiotic recombination, we examined the
237 localization of DMC1 on surface-spread chromosomes of spermatocytes,
238 together with SYCP3 as a marker for the progression of meiotic prophase I. As
239 shown previously [77-79], in control spermatocytes, DMC1 foci appear in leptonema,
240 peak in their number at early zygonema, and gradually decrease throughout
241 zygonema (Fig. 2a, b). In *Fignl1* cKO, DMC1 foci followed similar kinetics as seen
242 in controls. However, at any stage, the number of DMC1 foci in *Fignl1* cKO was
243 more than that in controls. In early zygonema, ~500 DMC1 foci (449±89 foci) are
244 observed in *Fignl1* cKO, which is 2.3-fold more than in controls (194±32 foci).
245 DMC1-focus number in *Fignl1* cKO clearly increased through meiotic prophase I
246 progression. In late zygonema, the number of DMC1 foci in *Fignl1* cKO was
247 reduced by half of that in early zygonema (220±70 foci compared to 449±89 foci),
248 indicating a turnover of the foci. These results suggest that FIGNL1 suppresses
249 excess DMC1 focus formation and/or timely progression of DMC1-mediated
250 recombination.
251 In *Fignl1* cKO spermatocytes, we always observed two populations: cells
252 with a high number of DMC1 foci and cells with a similar number of foci to controls.
253 We assumed that the latter is *Fignl1*$^{flox/\Delta}$ cells where Stra8-Cre recombinase failed
254 excision of the *Fignl1*$^{\Delta}$ allele. Note that we included these foci for our
255 quantification and that this population becomes an internal control for our analysis.
256
257 **Compromised meiotic recombination in *Fignl1* cKO**
258 ssDNA-binding proteins such as RPA and MEIOB-SPATA22 play a role in the
259 early/middle stage of meiotic recombination both before and after the DMC1
260 assembly. We examined the localization of RPA2, a subunit of RPA, on meiotic
261 chromosomes. In control spermatocytes, RPA2 foci appear from leptonema with
262 200-300 foci on average in mid/late leptonema (223±73 foci; Fig. 3a, b). The
263 number of RPA2 foci increased up to ~400 foci in zygonema (376±45 foci in mid-
264 zygonema) and persisted throughout zygonema (332±59 foci in late zygonema).
265 The RPA2-focus number in *Fignl1* cKO mid/late leptonema increased up to 300-

266 400 foci (368±100 foci) and a similar number persisted in the early zygotene
267 stage (409±59 foci). Different from control mid/late leptonema where the RPA2-
268 focus number is ~2-fold more than the DMC1 focus number (223±73 RPA2 foci
269 and 96±57 DMC1 foci), the number of RPA2 foci in *Fignl1* cKO is comparable to
270 that of DMC1 foci (368±100 RPA2 foci and 369 ±156 DMC1 foci). The number of
271 RPA2 foci in *Fignl1* cKO gradually decreased from mid-zygonema and was
272 significantly lower than controls in late zygonema (281±48 foci compared to
273 332±59 in controls; $p<0.0001$, Mann-Whitney *U*-test; Fig. 3b), suggesting a role
274 of FIGNL1 in the dynamic behavior of an RPA-associated recombination event.
275 We also analyzed the histone γH2AX staining as a marker of DSB formation and
276 its repair. Interestingly, *Fignl1* cKO spermatocytes with increased RPA2 foci
277 showed a similar or slightly reduced intensity of γH2AX from leptonema to the late
278 zygonema stage compared to controls (Extended Data Fig. 2a, b).
279 In meiotic recombination, cytological analyses showed that RPA2 foci
280 persist longer than DMC1/RAD51 foci from mid/late zygonema to early/mid
281 pachynema, suggesting a role of RPA in a late stage of meiotic recombination [80].
282 In zygonema (from early zygonema), foci containing the MutSγ complex with
283 MSH4 and MSH5 appear specifically on synapsed regions and show similar
284 behavior to RPA on meiotic chromosomes to regulate late recombination events
285 [81]. We studied MSH4 localization and observed the reduced MSH4 foci in *Fignl1*
286 cKO in mid/late zygonema (50±22 foci versus 107±47 foci in controls; Fig. 3c, d).
287 Given a possibility that the reduction in MSH4-focus number is an indirect
288 consequence of synapsis defects in *Fignl1* cKO, we also analyzed the density of
289 MSH4 foci per unit length of SC. MSH4-focus number and SC length (total
290 SYCP1 length) showed a linear relationship in control mid-zygonema ($r$=0.89; Fig.
291 3e). In *Fignl1* cKO, a correlation between MSH4-focus number and SC length
292 was also positive, but lower than in controls ($r$=0.58). Importantly, the density of
293 MSH4 foci per unit length of SC is reduced in *Fignl1* cKO relative to controls
294 (0.73±0.22 foci per μm of SC versus 0.98±0.18 foci per μm of SC in controls; Fig.
295 3f). These suggest that FIGNL1 is required for efficient loading of MSH4 for
296 meiotic recombination and downstream events such as SC elongation.
297 Crossover formation is a key outcome of meiotic recombination. The
298 crossover sites on meiotic chromosomes are marked with MutLγ complex such
299 as MLH1 foci [82]. Control late pachytene cells show ~25 MLH1 foci per nucleus.
300 On the other hand, we could not detect any MLH1 foci on late
301 zygotene/pachytene-like chromosomes of *Fignl1* cKO spermatocytes (Extended

302 Data Fig. 2c). This is consistent with the observation that FIGNL1 is essential for
303 the progression of spermatocytes into a pachytene stage where MLH1 foci form.
304
305 **FIGNL1 promotes the disassembly of RAD51 in male meiosis**
306 In human cultured cells, FIGNL1 regulates RAD51 assembly [53, 62]. We examined
307 the localization of RAD51 on meiotic chromosomes. As reported previously [77-79],
308 in control spermatocytes, RAD51 foci are observed from mid/late leptonema and
309 peak in early zygonema, and then decrease toward pachynema (Fig. 2c, d). The
310 average number of RAD51 foci is 107±56 and 181±27 foci per nucleus in control
311 mid/late leptotene and early zygotene stages, respectively. As seen for DMC1,
312 we detected an increased number of RAD51 foci in *Fignl1* cKO cells. The average
313 number of RAD51 foci in early zygonema is 380±98 foci, which is more than twice
314 compared to that of controls (181±27 foci). The number of RAD51 foci in
315 zygonema is similar to that of DMC1 foci, though ~700 RAD51 foci were observed
316 in some nuclei. When the zygotene stage progressed from early to late, the
317 RAD51-focus number in *Fignl1* cKO gradually decreased as in controls. However,
318 even at late zygonema, we detected a significant increase in RAD51-focus
319 number in *Fignl1* cKO relative to controls (182±86 foci compared to 128±32 foci
320 in controls; $p$=0.0163, Mann-Whitney $U$-test; Fig. 2d). These results show that
321 FIGNL1 promotes the timely resolution of RAD51 ensembles during the zygotene
322 stage.
323
324 **Increased RAD51/DMC1 foci in early leptonema in *Fignl1* cKO**
325 In contrast to the zygotene stage where the numbers of DMC1 and RAD51 foci
326 are comparable, focus numbers of DMC1 and RAD51 were clearly different at
327 early leptonema only in *Fignl1* cKO (Fig. 2a-d). In mid/late leptonema when
328 DMC1 and RAD51 foci appear on elongating SYCP3 stretches in controls, the
329 number of DMC1 foci in *Fignl1* cKO is 369±156 foci per cell, which is about 3-4
330 times more of that in controls (96±57 foci). The number of RAD51 foci in mid/late
331 leptonema in *Fignl1* cKO is 387±134 foci, 3-4 times more than in controls (107±56
332 foci). In early leptonema, where SYCP3 short stretches are yet elongated, DMC1
333 and RAD51 foci rarely appear in control spermatocytes. However, *Fignl1* cKO
334 showed 355±178 RAD51 foci, which exceeded the number of DMC1 foci
335 (194±148 foci). These suggest that FIGNL1 suppresses the formation of excess
336 numbers of RAD51 and DMC1 foci in early meiosis I, and that, in the absence of
337 FIGNL1, RAD51 and DMC1 loading is uncoupled.

338

339 **Meiotic S-phase in *Fignl1* cKO accumulates RAD51/DMC1 foci**

340 In wild-type meiosis, the formation of both RAD51 and DMC1 foci is mediated by
341 SPO11-induced DSBs in leptonema [83, 84]. Increased number of RAD51 and
342 DMC1 foci on early leptotene chromosome of *Fignl1* cKO spermatocytes led us
343 to analyze preleptotene (meiotic S-phase) spermatocytes in order to characterize
344 the origin of excess RAD51/DMC1 foci in the absence of FIGNL1. For *in vitro*
345 labeling of DNA replication, we incubated testis cell suspension with EdU for 1
346 hour in a culture medium. The preleptotene spermatocytes, where a limited
347 number of SYCP3 short stretches forms along with a numerous number of
348 SYCP3 dots, were categorized into two classes: pan dotty staining of EdU in early
349 preleptonema and clustered dotty staining of EdU in mid/late preleptonema. In
350 controls, both early and mid/late preleptotene EdU-positive spermatocytes
351 showed very few foci of RAD51 (Fig. 4a, b). On the other hand, we could detect
352 RAD51 foci in EdU-positive spermatocytes of *Fignl1* cKO, indicating RAD51-
353 focus formation during the meiotic S phase. The number of RAD51 foci in the
354 meiotic S-phase is around 300 in focus-positive nuclei (298±110 foci and
355 337±108 foci in early and mid/late preleptonema, respectively), which is ~3/4 of
356 the RAD51 focus number in meiotic prophase I of *Fignl1* cKO mice, but ~1.5-fold
357 more of that in early zygonema of control mice (compare Figs. 2d and 4b). Some
358 RAD51 foci in the meiotic S-phase are colocalized with EdU dots/lines,
359 suggesting that RAD51 foci are associated with DNA replication. However, when
360 DNA replication labeling with another thymidine analog IdU was shortened for 10
361 min, most of the RAD51 foci did not colocalize with IdU foci (Extended Data Fig.
362 3a-c), though the degree of colocalization was significantly higher than random
363 colocalization (3.7±1.9% of IdU foci colocalized with RAD51 compared to
364 2.5±1.3%, $p$=0.0261, Mann-Whitney $U$-test; 9.1±4.5% of RAD51 foci colocalized
365 with IdU compared to 6.2±3.3%, $p$=0.0439, Mann-Whitney $U$-test; Extended Data
366 Fig. 3c). It is unlikely that RAD51 is frequently associated with ongoing DNA
367 replication in meiotic S-phase.

368 Further evaluation of DMC1 localization in *Fignl1* cKO revealed the
369 presence of preleptotene spermatocytes containing DMC1 foci (Fig. 4c, d). The
370 number of DMC1 foci in focus-positive nuclei is around 150 (136±71 foci and
371 164±70 foci in early and mid/late preleptonema, respectively), about half of
372 RAD51 foci in *Fignl1* cKO. Of note is that very few DMC1 foci were detected in
373 control preleptotene spermatocytes. This suggests that FIGNL1 limits the

374 assembly of mitotic recombination machinery with RAD51 on chromatin during
375 the meiotic S-phase as well as meiotic recombination machinery containing
376 DMC1.
377
378 **Uncoupled loading of RAD51 and DMC1 in *Fignl1* cKO spermatocytes**
379 Despite the overall increase in RAD51 and DMC1 focus numbers on any
380 analyzed stages of *Fignl1* cKO spermatocytes, ~2-fold more RAD51 foci
381 compared to DMC1 foci in preleptotene and early leptotene stages suggest
382 uncoupling of RAD51 and DMC1 loading onto chromosomes in the absence of
383 FIGNL1. Co-staining of RAD51 and DMC1 confirmed different kinetics of RAD51
384 and DMC1 in *Fignl1* cKO (Fig 2e, f, Extended Data Fig. 4); DMC1 focus numbers
385 gradually increase from preleptonema to late leptonema/early zygonema
386 (177±74, 325±136, and 407±69 foci in preleptonema, early leptonema, and late
387 leptonema/early zygonema, respectively; Fig, 2f), whereas RAD51 focus
388 numbers are nearly constant in those stages (399±120, 476±109, and 480±95
389 foci in preleptonema, early leptonema, and late leptonema/early zygonema,
390 respectively). Colocalization analysis revealed a gradual increase in the number
391 of RAD51-DMC1 co-foci as DMC1 foci increased. In preleptotene and early
392 leptotene spermatocytes, 50-60% of DMC1 foci colocalized with RAD51 foci
393 (57.0±10.6% and 53.1±11.0% in preleptonema and early leptonema,
394 respectively; Fig, 2g) and less than 40% of RAD51 foci colocalized with DMC1
395 foci (25.7±9.9% and 35.3±12.0% in preleptonema and early leptonema,
396 respectively). The degree of colocalization at these stages is significantly lower
397 than that in the late leptotene/early zygotene stage where comparable levels of
398 colocalization with controls were observed (65.8±10.1% and 67.2±7.6% of DMC1
399 foci colocalized with RAD51 in *Fignl1* cKO and controls, respectively; 56.2±9.6%
400 and 59.3±8.9% of RAD51 foci colocalized with DMC1 foci in *Fignl1* cKO and
401 controls, respectively; Fig. 2g). These suggest that coupled loading of RAD51
402 and DMC1 in meiotic S-phase and early meiotic prophase I is compromised in
403 *Fignl1* cKO spermatocytes. On the other hand, the fact that more than half of
404 DMC1 foci are colocalized with RAD51 in preleptonema suggests that DMC1
405 preferentially binds to meiotic chromatin where RAD51 is already bound.
406
407 **RAD51/DMC1-focus formation in *Spo11* KO *Fignl1* cKO spermatocytes**
408 Both RAD51 and DMC1 foci appear in the meiotic S-phase in *Fignl1* cKO
409 spermatocytes, which is much earlier than meiotic prophase I with programmed

410 DSB formation by SPO11. To examine whether RAD51/DMC1 focus formation in
411 *Fignl1* cKO mice is independent of meiotic DSB formation or not, we constructed
412 *Spo11* KO *Fignl1* cKO mice (*Spo11*$^{-/-}$ *Fignl1*$^{flox/\Delta}$ *Stra8-Cre*$^{+}$), which is defective in
413 SPO11-mediated DSB formation [83, 84]. As shown previously, spermatocytes from
414 control *Spo11* KO mice (*Spo11*$^{-/-}$ *Fignl1*$^{flox/\Delta}$) did not show any RAD51 foci on
415 meiotic chromosomes (Fig. 5a, b, Extended Data Fig. 5a). On the other hand,
416 spermatocytes from *Spo11* KO *Fignl1* cKO show on average 300-400 RAD51 foci
417 from leptotene to zygotene(-like) stages (407±77, 390±64, and 292±34 foci for
418 focus-positive nuclei in leptonema, early zygonema, and late zygonema,
419 respectively; Fig. 5b). Moreover, *Spo11* KO *Fignl1* cKO also accumulates DMC1
420 foci with similar numbers to RAD51 foci (374±108, 391±57, and 342±54 foci for
421 focus-positive nuclei in leptonema, early zygonema, and mid-zygonema,
422 respectively; Fig. 5c, d, Extended Data Fig. 5b). Comparable numbers of RAD51
423 and DMC1 foci between *Fignl1* cKO and *Spo11* KO *Fignl1* cKO indicate that a
424 large fraction of RAD51 and DMC1 foci on meiotic chromatin in the absence of
425 FIGNL1 is independent of SPO11, thus meiotic DSBs. Like *Spo11* KO, *Spo11*
426 KO *Fignl1* cKO spermatocytes lack pun-nuclear γH2AX staining (Extended Data
427 Fig. 5c, d), supporting the assembly of RAD51/DMC1 complexes in the absence
428 of endogenous DSBs. *Spo11* KO *Fignl1* cKO spermatocytes died in the
429 pachytene-like stage with the formation of the pseud-sex body (Extended Data
430 Fig. 5d) as seen in *Spo11* KO spermatocytes [83, 84]. We also detected
431 RAD51/DMC1 foci in preleptotene spermatocytes of *Spo11* KO *Fignl1* cKO mice
432 (Fig. 5f). This confirms that RAD51/DMC1 focus formation during meiotic S-phase
433 is independent of the SPO11 function. Importantly, the degree of RAD51-DMC1
434 colocalization from preleptonema to early zygonema in *Spo11* KO *Fignl1* cKO is
435 comparable to that in *Fignl1* cKO and more than half of DMC1 foci are colocalized
436 with RAD51 at those stages in *Spo11* KO *Fignl1* cKO (Fig. 5e-g). This suggests
437 that DMC1 preferentially binds to RAD51-bound meiotic chromatin, which is most
438 likely dsDNA.
439
440 **RAD51 binds to and persists on meiotic recombination sites in *Fignl1* cKO**
441 **spermatocytes**
442 As described above, the absence of FIGNL1 increases the SPO11-independent
443 formation of RAD51 and DMC1 foci in meiotic prophase I, some of which would
444 come from the meiotic S-phase. Comparable numbers of RAD51 and DMC1 foci
445 in the presence and absence of SPO11 (i.e., meiotic DSBs) sought us to check

446 whether RAD51/DMC1 can bind to meiotic recombination hotspots, especially
447 ssDNA. Chromatin immunoprecipitation followed by single-stranded DNA
448 sequencing (ChIP-SSDS) for RAD51 [85-87] revealed that in *Fignl1* cKO testes, like
449 in controls, RAD51 binds to recombination hotspots where DMC1 strongly binds
450 in wild-type testes (Fig. 6a, Extended Data Fig. 6a). Importantly, when RAD51
451 binding around hotspots is ranked based on the number of SPO11-oligos in wild-
452 type, a similar binding profile of RAD51 is seen between *Fignl1* cKO and controls,
453 with a small increase in RAD51 ChIP-SSDS signals in two out of three *Fignl1*
454 cKO mice (Fig. 6b, Extended Data Fig. 6b-d).
455 To address whether RAD51 persists on meiotic recombination sites in the
456 absence of FIGNL1, we also measured the colocalization frequency of RAD51
457 and RPA2 in mid/late zygonema, given that RPA2 localizes to recombination sites
458 even after RAD51/DMC1 disassembly in wild-type meiosis and can be a marker
459 of recombination sites on mid/late zygotene chromosomes. In control mid/late
460 zygotene spermatocytes, out of 234±44 RPA2 foci, 41±15 foci were colocalized
461 with RAD51 foci, which corresponds to 17.2±4.3% of RPA2 foci (Fig. 6c-e). *Fignl1*
462 cKO exhibited two classes of populations; one is similar to controls (~30%) and
463 the other shows 40-80% of colocalization, with 45.4±21.9% of RPA2 foci
464 colocalized with RAD51 for all populations. This is consistent with the idea that
465 RAD51 binds to ssDNA on meiotic recombination sites in the absence of FIGNL1
466 and suggests that RAD51 persists on RPA2-associated recombination sites.
467
468 ***Fignl1* deficiency rescues RAD51/DMC1 assembly defects in *Swsap1***
469 Our previous study in human cells showed that FIGNL1 antagonizes the function
470 of the RAD51 mediator, SWSAP1 [53]. In mouse male meiosis, SWSAP1 is
471 necessary for efficient RAD51/DMC1 focus formation [18, 53]. We tested the effect
472 of *Fignl1* cKO on RAD51/DMC1 assembly in *Swsap1* KO cells by generating
473 *Swsap1* KO *Fignl1* cKO male mice (*Swasp1*$^{-/-}$ *Fignl1*$^{flox/\Delta}$ *Stra8-Cre*$^{+}$). As reported
474 [18, 53], surface-spread chromosomes from *Swasp1* KO spermatocytes (*Swsap1*$^{-/-}$
475 *Fignl1*$^{flox/\Delta}$) showed a large reduction of RAD51 foci with 10-30 foci (~1/10 of
476 control *Fignl1*$^{flox/\Delta}$) in leptonema and zygonema (29±26, 22±15, and 20±14 foci in
477 leptonema, early zygonema, and mid zygonema, respectively; Fig. 7a, b). Like
478 *Fignl1* cKO, *Swsap1* KO *Fignl1* cKO spermatocytes showed an accumulation of
479 RAD51 foci on meiotic chromosomes. The number of RAD51 foci from leptonema
480 to mid-zygonema in *Swsap1* KO *Fignl1* cKO is very similar to that in *Fignl1* cKO
481 (320±217, 308±221, and 194±179 foci in *Swsap1* KO *Fignl1* cKO and 399±145,

482 377±98, and 282±91 foci in *Fignl1* cKO in leptonema, early zygonema, and mid
483 zygonema, respectively). This indicates that in mouse spermatogenesis without
484 FIGNL1, RAD51 assembly does not depend on SWSAP1. This is consistent with
485 the results in human cultured cells. On the other hand, in late zygonema, the
486 number of RAD51 foci in *Swsap1* KO *Fignl1* cKO was comparable to *Swsap1* KO
487 and much lower than that in *Fignl1* cKO (10±12, 7±8, and 189±79 foci in *Swsap1*
488 KO *Fignl1* cKO, *Swsap1* KO, and *Fignl1* cKO, respectively; Fig. 7b). This
489 suggests that only *Swsap1*$^{-/-}$ *Fignl1*$^{flox/\Delta}$ cells where Stra8-Cre recombinase failed
490 excision of *Fignl1*$^{flox}$ allele can progress into late zygotene stage in *Swsap1* KO
491 *Fignl1* cKO testes. Moreover, similar results were observed for DMC1; the
492 number of DMC1 foci in *Swsap1* KO *Fignl1* cKO was comparable to *Fignl1* cKO
493 (Fig. 7c, d). Thus, reduced DMC1-focus formation in *Swsap1* KO is also
494 suppressed by *Fignl1* cKO. It is likely that the activity of FIGNL1 to suppress
495 RAD51/DMC1 assembly is separable from its activity regulated by SWSAP1.
496
497 **FIGNL1 disrupts RAD51-dsDNA complex *in vitro***
498 We previously showed that FIGNL1 promotes the dissociation of RAD51 from
499 ssDNAs *in vitro* [53]. The above results in mouse spermatocytes suggest that
500 FIGNL1 can disrupt RAD51 filaments on chromosomal DNAs, both ssDNAs and
501 dsDNAs. To address whether FIGNL1 promotes the dissociation of RAD51
502 filaments on dsDNAs *in vitro*, we performed the electrophoretic mobility shift
503 assay (EMSA). First, we confirmed that a purified human FIGNL1ΔN, which lacks
504 N-terminal 284 amino acids [53], disrupted the pre-formed RAD51-ssDNA
505 complexes in the presence of ATP (Fig. 8a, b). Under this condition, FIGNL1ΔN
506 could disrupt ~30% of RAD51-ssDNA complex (24.6±6.9% of unbound DNAs
507 were increased to 42.9±2.1% by the addition of 1.2 μM of FIGNL1ΔN). When
508 FIGNL1ΔN was incubated with a pre-formed RAD51-dsDNA complex, the most
509 of dsDNA was recovered as an unbound form (25.8±11.1% of unbound DNAs
510 were increased to 80.0±11.6%). This suggests that FIGNL1ΔN could disrupt the
511 RAD51-dsDNA complex more efficiently than the RAD51-ssDNA complex *in vitro*,
512 supporting the *in vivo* results.
513
514 **Discussion**
515 In this study, we analyzed the role of FIGNL1 AAA+ ATPase, which plays a critical
516 role in homologous recombination in somatic cells, in mouse male meiosis. *Fignl1*
517 cKO mice accumulated RAD51/DMC1 on meiotic chromosomes with defective

518 chromosome synapsis. Our analysis revealed the dual function of FIGNL1 during
519 spermatogenesis (Fig. 8c). One is to promote meiotic recombination by regulating
520 the dissociation of RAD51/DMC1 ensembles on the ssDNA. The other is to
521 protect the genome by disrupting the non-functional form of RAD51/DMC1
522 ensembles on the dsDNA. Consistent with the idea, purified FIGNL1 can disrupt
523 the RAD51-dsDNA complex as well as the RAD51-ssDNA complex *in vitro*.
524 The same conclusion was obtained by Baudat's group by characterizing the
525 *Fignl1* cKO as well as *Flip* cKO (accompanying paper).
526
527 **FIGNL1 promotes the post-assembly stage of RAD51/DMC1 in meiotic**
528 **recombination**
529 In meiotic recombination, RAD51/DMC1 filaments on ssDNAs play a critical role
530 in homology search and strand exchange with homologous dsDNA, leading to
531 the formation of the D-loop, in which the 3'-OH end of invading strand becomes
532 a substrate for recombination-associated DNA synthesis. Biochemical analyses
533 showed that RAD51/DMC1-mediated D-loop is a poor substrate for *in vitro* DNA
534 synthesis by DNA polymerase $\delta$ and its accessory factors [88-90]. To promote
535 efficient DNA synthesis on the recombination intermediate, RAD51/DMC1 bound
536 to the intermediate should be removed by factors such as RAD54, a RAD51
537 remodeler [88-90]. Although the male KO mice for Rad54 and for both Rad54 and
538 Rad54B, a Rad54 paralog, are fertile, the cKO spermatocytes show abnormal
539 loading of RAD51 on chromosomes in pachynema and diplonema [60]. This is
540 consistent with the role of RAD54 in the post-assembly stage of RAD51 (DMC1
541 had not been analyzed in detail). Our *in vivo* and *in vitro* studies suggest the role
542 of FIGNL1 in the post-assembly stage of the RAD51/DMC1 filaments (this study).
543 It is likely that FIGNL1 disrupts not only RAD51 but also DMC1 filaments on
544 recombination intermediates for subsequent DNA synthesis [89, 91] (Fig. 8c). Post-
545 assembly role of FIGNL1 in RAD51-mediated homologous recombination was
546 reported previously in human cells with DNA damage [62]. Consistent with the post-
547 assembly role of FINGL1, *Fignl1* cKO spermatocytes reduce the formation of
548 MSH4 foci, which appears after the loading and dissociation of RAD51/DMC1 [81].
549 *Fignl1* cKO spermatocytes seem not to enter the pachytene stage for the loading
550 of the MutL$\gamma$ complex such as MLH1 and most *Fignl1* KO cells die around late
551 zygonema. The meiotic defects seen in *Fignl1* cKO are similar to those in the
552 mutants where RAD51/DMC1 foci are accumulated such as *Msh4*, *Msh5*, *Mcm8*,
553 *Trip13,* and *Mcmdc2* [92-98]. In mouse spermatocytes, FIGNL1 seems to promote

554 ZMM-dependent CO formation. This is different from the role of FIGNL1 ortholog,
555 FIGL1, in *A. thaliana*. *Arabidopsis FIGL1* mutant meiocytes showed normal or
556 slightly elevated CO formation [63, 64]. Indeed, the depletion of FIGL1 or its partner
557 FLIP suppresses reduced CO formation in the absence of pro-CO proteins, ZMM
558 [63, 64]. This suggests the role of plant FIGL1-FLIP as an anti-CO factor, which
559 disrupts early recombination intermediates such as RAD51/DMC1 filaments on
560 the ssDNA prior to or during the strand invasion.
561
562 **FIGNL1 disrupts non-productive RAD51 and DMC1 ensembles on duplex**
563 **DNAs**
564 RAD51(DMC1)-focus formation depends on exogenous genotoxic treatment or
565 SPO11-catalyzed DSB formation associated with the resection, thus the
566 formation of ssDNAs. The most striking phenotypes seen in *Fignl1* cKO
567 spermatocytes are the accumulation of RAD51 and DMC1 foci in unchallenged
568 meiotic S-phase cells and spermatocytes in the absence of SPO11. This
569 accumulation of RAD51/DMC1 foci in the absence of DSBs, therefore the
570 ssDNAs, could be simply explained by the non-specific assembly of
571 RAD51/DMC1 filaments on chromatin DNAs, thus the binding to dsDNA (Fig. 8c).
572 Interestingly, human RAD51 and DMC1 bind to both ssDNAs and dsDNA with
573 similar affinity *in vitro* [17, 99] and RAD51 bears an activity to remodel the
574 nucleosome upon the dsDNA binding [100-102]. On the other hand, *in vivo* DNA
575 binding of RAD51 and DMC1 is restricted to ssDNAs. How cells discriminate
576 ssDNAs among lots of competitors, dsDNAs, in the RAD51/DMC1 binding
577 remains unsolved. Based on the results described here, we propose that FIGNL1
578 actively dismantles RAD51 and DMC1 filaments on dsDNAs, which is otherwise
579 non-productive for the recombination and/or might become obstacles to
580 chromosomal events on duplex DNAs such as DNA replication, transcription, and
581 others. Indeed, Bishop and his colleagues reported activities of the RAD54
582 translocase family to remove RAD51 and DMC1 from dsDNAs. In yeast meiosis,
583 Spo11-independent focus formation of Dmc1, but not of Rad51, depends on
584 Tid1/Rdh54, a Rad54 homolog [103]. And mitotic spontaneous Rad51 focus
585 formation on yeast chromosomes is increased in the absence of three
586 translocases, Rad54, Tid1/Rdh54, and Uls1 [104]. Moreover, in unchallenged
587 human cells, the absence of two RAD54 family proteins RAD54 (or RAD54L) and
588 RAD54B leads to the accumulation of spontaneous RAD51 foci particularly when
589 RAD51 is over-expressed [105]. Further studies are necessary to reveal the

590 relationship between FIGNL1 and RAD54 translocases in the remodeling of
591 RAD51/DMC1 assembles on duplex DNAs.
592 One of the striking features of RAD51/DMC1 assembles on duplex DNAs is
593 that these ensembles are quite stable. The number of RAD51 in both meiotic S-
594 phase and early meiotic prophase I from early leptonema to early zygonema is
595 constant. Little increase in RAD51-focus number during early meiotic prophase I
596 suggest that spermatocytes show very limited additional assembly of RAD51 foci
597 during this stage. On the other hand, DMC1 shows a 2-fold increase in focus
598 number from early leptonema (and meiotic S-phase) to early zygonema. This
599 increase could be induced by SPO11-mediated DSBs. Interestingly, the
600 colocalization frequency of RAD51 with DMC1 in *Fignl1* cKO increased from
601 ~30% to ~60%, which is similar to the colocalization frequency seen in control
602 early zygonema, while the colocalization frequency of DMC1 with RAD51 is
603 nearly constant (with 60-70% frequency). This suggests that RAD51 ensembles
604 even on the dsDNA tend to recruit DMC1 to form co-ensembles.
605
606 **FIGNL1 antagonizes SWSAP1 for RAD51/DMC1 assembly on meiotic**
607 **chromosomes**
608 FIGNL1 shows antagonism to the RAD51 mediator. In humans, *FIGNL1*
609 depletion suppresses RAD51-assembly defect induced by the *SWSAP1*
610 depletion [53]. In meiosis of the *A. thaliana*, *FIGL1* (*A. thaliana FIGNL1*) and/or *FLIP*
611 deletion restores reduced RAD51/DMC1 focus formation in the mutants of the
612 *BRCA2* [67] as well as defective DMC1-focus formation in the mutant of the *SDS1*,
613 which promotes DMC1 assembly [63]. Given that *Swsap1* KO spermatocytes
614 reduced the RAD51 and DMC1 foci [18, 53], we asked whether *Fignl1* cKO could
615 also suppress these meiotic defects in *Swsap1* KO spermatocytes and found that
616 the number of both RAD51/DMC1 foci in *Swsap1* KO *Fignl1* cKO is similar to
617 those in *Fignl1* cKO. This is simply interpreted as, like in human cells, *Fignl1* cKO
618 suppresses RAD51/DMC1 assembly defect in *Swsap1* KO. However, at this point,
619 we do not know whether RAD51/DMC1 foci are associated with ssDNAs in
620 meiotic prophase I cells of *Swsap1* KO *Fignl1* cKO as shown in *Fignl1* cKO,
621 although it is likely. In addition, different from RAD51/DMC1 assembly on ssDNAs,
622 these suggest that RAD51/DMC1 assembly on dsDNAs in the absence of
623 FIGNL1 does not require the RAD51/DMC1 mediator, SWSAP1.
624

625 **Methods**
626
627 **Mice**
628 The care and use of mice in this study were performed under the guideline for
629 the proper conduct of animal experiments (Society Council of Japan). These
630 procedures were approved by the Institutional Animal Care Committee at Institute
631 for Protein Research, Osaka University (approval ID; 25-03-0).
632 All mice used in this study were congenic to the C57BL/6 background.
633 Genotyping of mice was performed by PCR on genomic DNA isolated from mice.
634 Primers used for genotyping are listed in Supplementary table 1. Mature adult
635 mice (8-20 weeks old) were used for experiments otherwise mentioned.
636 *Fignl1*$^{flox}$ allele was constructed by Cyagen Bioscience Co. Ltd. ES cells with
637 the *Fignl1*$^{flox}$ allele were injected into C57BL/6 albino blastocytes, which were
638 transplanted into CD-1 pseudo-pregnant female mice. The founder mice with the
639 correct *Fignl1*$^{flox}$ allele were backcrossed to C57BL/6 mice. *Fignl1*$^{+/\Delta}$ allele was
640 constructed by breeding *Fignl1*$^{flox/+}$ with *CAG-Cre* mice. *Stra8-Cre* transgenic
641 mice were previously described [106] and provided *by* the RIKEN Animal Resource
642 Center. *Spo11*$^{-/-}$ mouse was previously described [83] and *Spo11*$^{+/-}$ mice with a
643 mixed background of C57BL/6 and 129/SvJ were backcrossed to C57BL/6 mice
644 prior to experiments. *Swsap1*$^{-/-}$ mice were described in our previous study [53].
645
646 **Histology**
647 Testes from adult mice were fixed in 10% buffered formalin overnight at room
648 temperature, washed twice with PBS, and stored in 70% EtOH at 4ºC prior to
649 embedding in paraffin and sectioning. The sections of 5 μm thickness were
650 deparaffinized and stained with hematoxylin and eosin (H&E).
651
652 **Spermatocyte chromosome spreads**
653 Surface-spread chromosomes of spermatocytes were prepared as described
654 previously [107, 108] with slight modification. Testes were dissected, the tunica
655 albuginea was removed, and adherent extra-tubular tissues were removed by
656 rinsing and dissociating seminiferous tubules in PBS using a pair of 25-gauge
657 needles in a 35 mm petri dish (Corning, 430165). Dissociated seminiferous
658 tubules were incubated in hypotonic extraction buffer (30 mM Tris-HCl pH 8.0, 50
659 mM sucrose, 17 mM trisodium citrate dihydrate, 5 mM EDTA, 0.5 mM
660 Dithiothreitol (DTT) and 0.5 mM phenylmethylsulphonyl fluoride (PMSF), pH 8.2-

661 8.3; HEB) for 15-45 min at room temperature. After quickly rinsing seminiferous
662 tubules in 100 mM sucrose, some tubules were placed in 40 μl of 100 mM sucrose
663 on a glass depression slide. Tubules were torn to pieces using two fine forceps,
664 and pieces of tubular remnants were removed. The volume was increased to 40
665 μl by adding 100 mM sucrose and the cell suspension was made by pipetting. A
666 clean glass slide (Matsunami, MAS-01) was dipped into freshly made 1%
667 paraformaldehyde (PFA) solution pH 9.2 (pH set by 1.25 M sodium borate)
668 containing 0.15% Triton X-100 in a 50 ml Falcon tube, and then extra 1% PFA /
669 0.15% Triton X-100 solution was removed. 20 μl of cell suspension was placed
670 at the upper right corner of the slide and was slowly dispersed in horizontal and
671 vertical directions several times to make cells homogenous on the slide. Slides
672 were placed and dried in a closed humid chamber with hot tap water overnight at
673 room temperature, followed by drying with lids ajar for 3 h and then with lids
674 removed for 1-2 hr. Slides were washed once for 5 min in deionized water and
675 twice for 5 min in 0.4% DryWell (Fujifilm) in a coplin jar and air-dried at room
676 temperature. Slides were either directly processed for immunostaining as below
677 or stored in aluminum foil at -80$^{o}$C prior to immunostaining.
678 For the preparation of testicular cell suspension, testes were dissected, the
679 tunica albuginea was removed, and seminiferous tubules were transferred into 1
680 ml of testis cell isolation medium (104 mM NaCl, 45 mM KCl, 1.2 mM $MgSO_4$, 0.6
681 mM $NaHPO_4$, 0.15 (w/v) glucose; TIM) containing 2 mg of collagenase
682 (Worthington, LS004186) for incubation at 32$^{o}$C for 55 min with shaking at 53 rpm.
683 Tubules were pelleted by centrifugation at 1,220 x *g* for 2 min at room temperature,
684 washed three times with 3 ml of TIM, and suspended in 1 ml of TIM containing
685 0.7 mg of Trypsin (Worthington, LS003740) and 4 μg of DNase I (Roche, 104159)
686 for incubation at 32$^{o}$C for 15 min with shaking at 53 rpm. Trypsinization was
687 stopped by adding 5 mg of Trypsin inhibitor (Sigma, T9003) and 10 μg of DNase
688 I, and cells were separated by pipetting and filtered through a 70 μm cell strainer
689 (Corning, 431751). TIM was added up to 7.5 ml and cells were pelleted by
690 centrifugation at 1,220 x *g* for 3 min at room temperature. After the removal of
691 supernatants, 0.75 μg of DNase I was added, cell pellets were dislodged and
692 suspended in 7.5 ml of TIM for cell counting. Pelleting was repeated, and the cell
693 pellet was suspended in 0.75 μg of DNase I and PBS (Nakarai, 14249-24) to 1
694 x$10^6$ cell/ml. 1 ml of cell suspension was then transferred to a 1.5 ml tube and
695 centrifuged at 200 x *g* for 5 min at room temperature. After carefully removing the
696 supernatant, cells were suspended in 30 μl of HEB and incubated for 15-45 min

697 at room temperature. 30 µl of 100 mM sucrose was added, and 20 µl of cell
698 suspension was placed on a clean glass slide (Matsunami, MAS-01) coated with
699 100 µl of freshly made 1% paraformaldehyde (PFA) solution pH 9.2 (pH set by
700 1.25 M sodium borate) containing 0.15% Triton X-100. Cells were slowly
701 dispersed in horizontal and vertical directions several times to get homogenous
702 on the slide. Slides were placed and dried in a closed humid chamber with hot
703 tap water overnight at room temperature, followed by drying with lids ajar for 3 h
704 and then with lids removed for 1-2 h. Slides were dried, washed, and stored as
705 described above.
706
707 **Immunofluorescence staining**
708 Slides were rehydrated with Tris-buffered saline (TBS) pH 8.0 containing 0.05%
709 of Triton X-100 (TBST) for 3 min, blocked twice with blocking buffer (1% normal
710 goat or donkey serum, 3% bovine serum albumin (BSA), 1x TBS pH 8.0, 0.05%
711 of Triton X-100, 0.05% sodium azide) for 15 min at room temperature and
712 incubated with primary antibodies in antibody dilution buffer (10% normal goat or
713 donkey serum, 3% BSA, 1x TBS pH 8.0, 0.05% of Triton X-100, 0.05% sodium
714 azide) in a humid chamber overnight at room temperature. Slides were quickly
715 rinsed with TBST, washed twice with TBST for 5 min, blocked twice with blocking
716 buffer for 15 min at room temperature, and incubated with secondary antibodies
717 in antibody dilution buffer in a humid chamber for 1 h at 37°C. Slides were quickly
718 rinsed with TBST, washed three times with TBST for 5 min, washed once with
719 Milli-Q water for 2 min, and air-dried before mounting with ProLong Diamond
720 Antifade Mountant (Thermo Fisher Scientific, P36970). For detection of IdU,
721 rehydrated slides were denatured with 4N HCl for 10 min at room temperature
722 before blocking. EdU was detected using Click-iT EdU Imaging Kit with Alexa
723 Fluor 647 azides according to the manufacturer's instruction (Invitrogen). All
724 primary and secondary antibodies used are listed in Supplementary table 2.
725
726 **Testicular cell squashes**
727 Testes were dissected, the tunica albuginea was removed, and adherent extra-
728 tubular tissues were removed by rinsing and dissociating seminiferous tubules in
729 PBS using a pair of 25-gauge needles in a 35 mm petri dish (Corning, 430165).
730 Dissociated seminiferous tubules were fixed in freshly prepared 2%
731 formaldehyde containing 0.1% Triton X-100 for 10 min at room temperature.
732 Small pieces of tubules were placed on a clean glass slide (Matsunami, MAS-01),

733 torn using two fine forceps, and squashed under a coverslip with pressure from
734 the blunt end of pencil followed by a thumb. Slides were frozen briefly in liquid
735 nitrogen and either directly processed for immunostaining or stored at -80°C prior
736 to immunostaining. After the removal of coverslips, slides were washed three
737 times with PBS for 5 min and immunostaining was performed as described above.
738

739 **Image acquisition**

740 Images of mouse spermatocyte spreads testicular cell squashes were acquired
741 using a computer-assisted fluorescence microscope system (DeltaVision;
742 Applied Precision) with a 60× NA 1.4 oil immersion objective. Image
743 deconvolution was performed using an image workstation (SoftWorks; Applied
744 Precision) and afterward processed using Imaris (Oxford Instruments, UK) and
745 Photoshop (Adobe, USA) software tools. Images in each figure are matched
746 exposure.
747

748 **Image analysis**

749 Comparisons were made between animals that were either littermate or matched
750 by age. Single cells were manually cropped, and numbers of foci were counted
751 by the auto-thresholding signal intensity in Imaris software (Oxford Instrument)
752 and clear foci that were missed by auto-thresholding, especially adjacent foci,
753 were manually counted. Signal intensities were measured using Image J software
754 by subtracting signal intensities of single cells from those of regions of interest
755 (ROIs) manually drawn next to cells as backgrounds.
756 Meiotic prophase I stages on spermatocyte spreads were defined by
757 SYCP3 and SYCP1 staining using standard criteria. Leptonema was defined by
758 short SYCP3 stretches without evidence of synapsis determined by SYCP1
759 staining. Zygonema was defined by longer stretches of SYCP3 with various
760 degrees of synapsis: early, mid- and late zygonema was defined by having <25%,
761 25-75%, and >75% of synapsis, respectively. Pachynema was defined by the full
762 synapsis of all autosomes. Diplonema was defined by de-synapsis beginning
763 from mostly the middle of chromosomes with various degrees of residual
764 synapsis. Preleptonema was defined by very short SYCP3 stretches with EdU or
765 IdU-positive staining.
766

767 **EdU incorporation**

768 1 ml of 1 x$10^6$ cell/ml testicular cell suspension in PBS was centrifuged at 200 x

769 *g* for 5 min at room temperature, and after removal of the supernatant, cells were
770 suspended in 500 μl of D-MEM (Wako, 044-29765) / 10% FBS containing 10 μM
771 EdU. After incubation at 37°C for 1 h in a well of a 12-well dish (Violamo), cells
772 were pelleted by centrifugation at 200 x *g* for 5 min at room temperature, washed
773 in 1 ml of PBS once, and suspended in 30 μl HEB for incubation for 15-30 min at
774 room temperature. After adding 30 μl of 100 mM sucrose, cells were fixed, and
775 the slides were dried, washed, and stored as described above.
776
777 **IdU pulse incorporation**
778 1 ml of 1 x$10^6$ cell/ml testicular cell suspension in PBS was centrifuged at 200 x
779 *g* for 5 min at room temperature, and after removal of the supernatant, cells were
780 suspended in 500 μl of D-MEM (Wako, 044-29765) / 10% FBS containing 20 μM
781 IdU (Sigma, I7125). After incubation at 37°C for 10 min in a well of a 12-well dish
782 (Violamo), cells were subjected to chromosome spreads as described above.
783
784 **Rad51 Chromatin immuno-precipitation – single-stranded DNA sequencing**
785 **(ChIP-SSDS)**
786 ChIP was performed as described previously [85]. One testis from the control and
787 a pair of testes from *Fignl1* cKO mice (14-18 weeks) were dissected, the tunica
788 albuginea was removed, and seminiferous tubules were transferred into 10 ml of
789 1% formaldehyde (Pierce, 28908) in PBS (Nakarai, 14249-24) and immediately
790 homogenized in a Dounce homogenizer with 20 strokes of the tight-fit pestle. The
791 homogenate was passed through a 70 μm cell strainer (Falcon, 352350), and
792 after a total of 10 min of incubation at room temperature, crosslinking was
793 quenched by adding 2.5 M glycine to a final concentration of 125 mM. After 5 min
794 of incubation at room temperature, cells were pelleted by centrifugation at 900 x
795 *g* for 5 min at 4°C, washed once with 10 ml of cold PBS, and suspended in 1 ml
796 of cold PBS. The cell suspension was transferred to a 1.5 ml tube, centrifuged at
797 900 x *g* for 5 min at 4°C, and after removal of the supernatant, the cell pellet was
798 snap-frozen on liquid nitrogen and stored at -80°C. The frozen cell pellet was
799 suspended in 500 μl of cell lysis buffer (0.25% Triton X-100, 10 mM EDTA, 0.5
800 mM EGTA, 10 mM Tris-HCl pH 8.0) supplemented with protease inhibitor (Roche,
801 04693159001), incubated for 10 min on ice, centrifuged at 300 x *g* for 3 min at
802 4°C, and the nuclei pellet was resuspended in 500 μl of lysis wash buffer (200
803 mM NaCl, 1 mM EDTA, 0.5 mM EGTA, 10 mM Tris-HCl pH 8.0) supplemented
804 with protease inhibitor. After centrifugation at 300 x *g* for 3 min at 4°C, the nuclei

805 pellet was resuspended in 200 μl of RIPA buffer (10 mM Tris-HCl pH 8.0, 1 mM
806 EDTA, 0.5 mM EGTA, 1% Triton X-100, 0.1% sodium deoxycholate, 0.1% SDS,
807 140 mM NaCl) supplemented with protease inhibitor and split into two ~130 μl
808 aliquots and sonicated on the Covaris M220 for 5 min 30 sec at 5-9°C with a
809 setting of Peak Power 50.0, Duty Factor 20.0, and Cycles/Burst 200. Sheared
810 nuclei were combined, and after adding 700 μl of RIPA buffer, centrifuged at
811 15,000 rpm for 15 min at 4°C to remove insoluble debris. 800 μl of the chromatin-
812 containing supernatant was mixed with 50 μl of Dynabeads protein G bound to
813 9.7 μg of RAD51 antibody (Novus, NB100-148) and incubated overnight on a
814 rotating wheel at 4°C for immunoprecipitation. Beads were washed once with 1
815 ml of cold ChIP wash buffer 1 (0.1% SDS, 1% Triton X-100, 2 mM EDTA, 20 mM
816 Tris-HCl pH 8.0, 150 mM NaCl), 1 ml of cold ChIP wash buffer 2 (0.1% SDS, 1%
817 Triton X-100, 2 mM EDTA, 20 mM Tris-HCl pH 8.0, 500 mM NaCl), 1 ml of cold
818 ChIP wash buffer 3 (0.25 M LiCl, 1% NP-40, 1% sodium deoxycholate, 1 mM
819 EDTA, 10 mM Tris-HCl pH 8.0), and twice with 1 ml of cold TE (1 mM EDTA and
820 10 mM Tris-HCl pH 8.0), followed by elution with 100 μl of elution buffer (0.1 M
821 $NaHCO_3$ and 1% SDS) for 30 min at 65°C with vortexing every 10 min. The elutes
822 were incubated overnight at 65°C for de-crosslinking, neutralized by adding 4 μl
823 of 1M Tris-HCl (pH 6.5) and 2 μl of 0.5 M EDTA, and RNA was digested by adding
824 2 μl of 10 mg/ml RNase-A and incubation for 15 min 37°C. After adding 5 μl of 10
825 mg/ml Proteinase-K (Wako, 165-21043) and incubation for 1 h at 55°C, DNA was
826 purified using QIAquick PCR Purification Kit (QIAGEN).
827 SSDS was performed as described previously (Brick et al., 2018). 7-10 ng
828 of ChIP DNA was further sonicated on the Covaris M220 for 8 min 30 sec at room
829 temperature with a setting of Peak Power 75.0, Duty Factor 10.0, and
830 Cycles/Burst 200, followed by end-repair and dA-tailing using ChIP-Seq Library
831 Prep Reagent Set for Illumina (NEB, E6200L). DNA was incubated for 3 min at
832 95°C and returned to room temperature for kinetic enrichment for single-stranded
833 DNA. After adapter ligation using IDT for Illumina TruSeq DNA UD Indexes
834 (Illumina, 20022370), SSDS libraries were amplified during 15 cycles of PCR
835 using TruSeq DNA Nano LP (Illumina, 20016328), purified with AMPureXP beads
836 (Beckman Coulter, A63880), and sequenced on HiSeq2500 in the rapid mode in
837 a 50 bp PE run. Around 70 million paired reads were generated per sample.
838 A published bioinformatic pipeline (https://nf-co.re/ssds/dev) was run for the
839 resulting reads for the identification of single-stranded sequences and mapping
840 to the mm10 genome [109]. Heatmaps were generated using Deeptools [110].

841
842 **Western blot**
843 Testes were dissected, the tunica albuginea was removed, and seminiferous
844 tubules were snap frozen on liquid nitrogen and stored at -80°C before cell lysis.
845 Tubules from either one testis (*Fignl1*$^{+/+}$ *Stra8-Cre*$^{+}$ and *Fignl1*$^{flox/\Delta}$) or two testes
846 (*Fignl1*$^{flox/\Delta}$ *Stra8-Cre*$^{+}$) were homogenized in 1 ml of RIPA buffer (50 mM Tris-HCl
847 pH 7.5, 150 mM NaCl, 1 mM EDTA, 1% NP-40, 0.5% sodium deoxycholate, 0.1%
848 sodium dodecyl sulfate (SDS)) supplemented with protease inhibitor (Roche,
849 04693159001)) on ice, incubated for 15 min on ice, sonicated with a Bioruptor for
850 30 min (30 cycles of 30 sec ON / 30 sec OFF) at 4°C with a setting of High
851 intensity, and incubated for 15 min on ice. The samples were centrifuged at
852 14,000 rpm for 15 min at 4°C and the supernatants were collected as whole-testis
853 extracts. Protein concentrations were measured by Brad-ford assay and the
854 concentrations between samples were made constant by adding RIPA buffer
855 supplemented with protease inhibitor. Whole-testis extract was mixed with 4x
856 SDS-PAGE loading buffer (250 mM Tris-HCl pH 6.8, 8% SDS, 40% glycerol, 572
857 mM β-mercaptoethanol, 0.05% bromophenol blue) and boiled for 5 min at 100ºC
858 and subjected to immunoblotting.
859 Protein samples were separated on 10% gels by SDS-PAGE and
860 transferred to PVDF membranes by wet transfer method in Towbin buffer (25 mM
861 Tris, 192 mM glycine, 20% ethanol) at 60 V for 150 min at 4°C. Membranes were
862 blocked with PBS containing 2.5% non-fat milk for 1 h at room temperature and
863 incubated with primary antibodies in 2.5% non-fat milk in PBS overnight at 4°C.
864 Membranes were washed three times with PBS containing 0.05% Tween-20
865 (PBST) for 10 min and incubated with HRP-conjugated secondary antibodies in
866 PBST for 1 h at room temperature. Membranes were washed three times with
867 PBST for 10 min and the signal was developed by ECL Prime Western Blotting
868 Detection Reagent (Amersham) and detected by ImageQuant LAS4000 (GE
869 Healthcare).
870
871 **Antibody generation**
872 His-tagged mouse SYCP3 was overexpressed from pET28c-SYCP3 plasmid by
873 the addition of 0.2 mM IPTG in BL21(DE3) at 37°C for 4 h. Cell extracts were
874 prepared in Lysis buffer (50 mM Tris-HCl pH 7.5, 500 mM NaCl) by sonication
875 and the supernatants were collected after centrifugation at 20,400 x *g* for 30 min
876 at 4°C. After adding Tween-20 to a final concentration of 0.2%, the cell lysates

877 were incubated with Ni-NTA Agarose (QIAGEN) for 2 h at 4°C and the lysate-
878 resin slurry was washed in Lysis buffer containing 50 mM Imidazole, 100 mM
879 Imidazole, 300 mM Imidazole. Ni-NTA-bound His-SYCP3 was eluted in Lysis
880 buffer containing 3M Imidazole and 3M Urea (elution 1) by incubation for 1 h at
881 4°C and in Lysis buffer containing 0.1% SDS (elution 2) by incubation for 30 min
882 at room temperature. Elution 2 was concentrated using MICROCON Centrifugal
883 Filter Device YM-10 (Millipore) and subjected to immunization to a rat.
884
885 **Purification of RAD51 and FINGL1ΔN**
886 GST-tagged human FIGNL1ΔN (N-terminal 284 aa deletion) was overexpressed
887 from pGEX-6P-1-*FignI1ΔN* plasmid by the addition of 0.25 mM IPTG in
888 BL21(DE3) pLysS at 30°C for overnight. Cell extracts were prepared in Lysis
889 buffer (25 mM Tris-HCl pH 7.6, 150 mM NaCl, 10% Glycerol, 1 mM DTT) and
890 GST-FIGNL1ΔN was recovered by GSTrap HP column (Cytiva). FIGNL1ΔN was
891 eluted from the GSTrap column by the cleavage of GST tag by Prescission
892 protease (#27-0843-01, Cytiva) in SP buffer (20 mM HEPES-NaOH pH 7.5, 10%
893 Glycerol, 1 mM DTT) supplemented with 100 mM NaCl. FIGNL1ΔN was further
894 purified by HiTrap SP column (Cytiva) with a linear gradient of 100 mM-1M in SP
895 buffer. The peak fractions are dialyzed against SP buffer supplemented with 100
896 mM NaCl, concentrated with Amicon Ultra 30K (Millipore), and stored at -80°C.
897 Human RAD51 was purified as described previously using pET-HsRad51 plasmid
898 [111].
899
900 **Electrophoresis mobility shift assay (EMSA)**
901 Double-stranded DNA substrate was prepared by annealing 5'-Cy5-labeled, 40-
902 mer oligo DNA (Oligo 1, Cy5-
903 TAATACAAAATAAGTAAATGAATAAACAGAGAAAATAAAG, IDT) and its
904 complementary DNA (Oligo 2,
905 CTTTATTTTCTCTGTTTATTCATTTACTTATTTTGTATTA, Fasmac). Oligo 1
906 was used as an ssDNA substrate. For the assay, DNA (0.8 μM in bp/nt) was pre-
907 incubated with 1 μM of RAD51 in 10 μl of the buffer (20 mM HEPES-NaOH pH7.5,
908 100 ug/ml BSA, 1 mM DTT, 10 mM $MgCl_2$, 2 mM ATP) at 37°C for 5 min to form
909 RAD51-DNA complex. Then the indicated concentration of FIGNL1ΔN was added
910 to the reaction and further incubated at 37°C for 15 min. In the control reaction
911 without FIGNL1ΔN, the same volume of dialysis buffer was added instead of the
912 protein. DNA-protein complexes were analyzed using 8% native polyacrylamide

913 gel electrophoresis with 1×TBE. Cy5-labelled DNA was visualized by LAS4000
914 (GE healthcare) and unbound DNA was quantified using ImageQuant TL (GE
915 healthcare). Images were further processed to adjust brightness using Photoshop
916 (Adobe, USA) software.
917
918 **Statistical analysis and reproducibility**
919 Statistical analyses were performed using Graphpad Prism software v.9 and R
920 version 4.2.2 (https://www.r-project.org). Bars in figures and values in
921 manuscripts indicate means ± standard deviations (SDs) otherwise mentioned.
922 Statistic parameters and tests and sample sizes are described in the figures
923 and/or figure legends. Sample sizes were not predetermined using any statistical
924 tests.
925 At least two animals of each genotype were analyzed and similar results
926 were obtained otherwise mentioned. Three independent experiments were
927 performed for biochemical analysis.
928
929 **Data availability**
930 The raw and processed sequencing data have been deposited in the Gene
931 Expression Omnibus (GEO) repository under accession number GSE227944.
932
933 **Acknowledgments**
934 We thank Drs. F. Baudat and B. de Massy for sharing unpublished results. We
935 acknowledge Drs. F. Pratto and V. Jayakumar for SSDS analysis. We are grateful
936 to Ms. S. Kondo for the generation of anti-SYCP3. We acknowledge Drs. S.
937 Keeney, Y. Fujiwara, and K. Ishiguro for *spo11* mice and Dr. H. Kurumizaka for
938 the RAD51 expression plasmid. We are also indebted to members of the
939 Shinohara lab, particularly Ms. S. Aoyama, A. Maeda, C. Watanabe, and S.
940 Hashimoto for mouse care. This work was supported by JSPS KAKENHI Grant
941 Numbers; 19H00981 to A.S., 20K15716 and 16H06279 (PAGS) to M.I., and
942 19H03157 to A.F.
943
944 **Author contributions**
945 M.I. and A.S. conceived and designed the experiments. M.I. performed all
946 experiments on mouse meiosis. M.I., Y.F., and A.T. analyzed SSDS data. A.F.
947 performed biochemical experiments. K.M. set up Fignl1 mice. M.I. and A.S.
948 analyzed the data. A.S. prepared the original draft and wrote the manuscript with

help from M.I.

**Competing interest**

The authors declare no competing interests.

954 **References**

955


956 1. Sonoda, E. *et al.* Rad51-deficient vertebrate cells accumulate
957 chromosomal breaks prior to cell death. *EMBO J* **17**, 598-608 (1998).
958 2. Tashiro, S., Walter, J., Shinohara, A., Kamada, N. & Cremer, T. Rad51
959 accumulation at sites of DNA damage and in postreplicative chromatin. *J*
960 *Cell Biol* **150**, 283-291 (2000).
961 3. Mason, J.M., Chan, Y.L., Weichselbaum, R.W. & Bishop, D.K. Non-
962 enzymatic roles of human RAD51 at stalled replication forks. *Nat Commun*
963 **10**, 4410 (2019).
964 4. Schlacher, K. *et al.* Double-strand break repair-independent role for
965 BRCA2 in blocking stalled replication fork degradation by MRE11. *Cell* **145**,
966 529-542 (2011).
967 5. Feretzaki, M. *et al.* RAD51-dependent recruitment of TERRA lncRNA to
968 telomeres through R-loops. *Nature* **587**, 303-308 (2020).
969 6. Ogawa, T., Yu, X., Shinohara, A. & Egelman, E.H. Similarity of the yeast
970 RAD51 filament to the bacterial RecA filament. *Science* **259**, 1896-1899
971 (1993).
972 7. Shinohara, A., Ogawa, H. & Ogawa, T. Rad51 protein involved in repair
973 and recombination in S. cerevisiae is a RecA-like protein. *Cell* **69**, 457-470
974 (1992).
975 8. Sung, P. Catalysis of ATP-dependent homologous DNA pairing and strand
976 exchange by yeast RAD51 protein. *Science* **265**, 1241-1243 (1994).
977 9. Sung, P. & Robberson, D.L. DNA strand exchange mediated by a RAD51-
978 ssDNA nucleoprotein filament with polarity opposite to that of RecA. *Cell*
979 **82**, 453-461 (1995).
980 10. Jensen, R.B., Carreira, A. & Kowalczykowski, S.C. Purified human BRCA2
981 stimulates RAD51-mediated recombination. *Nature* **467**, 678-683 (2010).
982 11. Zhao, W. *et al.* BRCA1-BARD1 promotes RAD51-mediated homologous
983 DNA pairing. *Nature* **550**, 360-365 (2017).
984 12. New, J.H., Sugiyama, T., Zaitseva, E. & Kowalczykowski, S.C. Rad52
985 protein stimulates DNA strand exchange by Rad51 and replication protein
986 A. *Nature* **391**, 407-410 (1998).
987 13. Shinohara, A. & Ogawa, T. Stimulation by Rad52 of yeast Rad51-mediated
988 recombination. *Nature* **391**, 404-407 (1998).
989 14. Van Dyck, E., Stasiak, A.Z., Stasiak, A. & West, S.C. Binding of double-

990 strand breaks in DNA by human Rad52 protein. *Nature* **398**, 728-731
991 (1999).
992 15. Akamatsu, Y., Dziadkowiec, D., Ikeguchi, M., Shinagawa, H. & Iwasaki, H.
993 Two different Swi5-containing protein complexes are involved in mating-
994 type switching and recombination repair in fission yeast. *Proc Natl Acad*
995 *Sci U S A* **100**, 15770-15775 (2003).
996 16. Tsai, S.P. *et al.* Rad51 presynaptic filament stabilization function of the
997 mouse Swi5-Sfr1 heterodimeric complex. *Nucleic Acids Res* **40**, 6558-
998 6569 (2012).
999 17. Masson, J.Y. *et al.* Identification and purification of two distinct complexes
1000 containing the five RAD51 paralogs. *Genes Dev* **15**, 3296-3307 (2001).
1001 18. Abreu, C.M. *et al.* Shu complex SWS1-SWSAP1 promotes early steps in
1002 mouse meiotic recombination. *Nat Commun* **9**, 3961 (2018).
1003 19. Liu, T., Wan, L., Wu, Y., Chen, J. & Huang, J. hSWS1.SWSAP1 is an
1004 evolutionarily conserved complex required for efficient homologous
1005 recombination repair. *J Biol Chem* **286**, 41758-41766 (2011).
1006 20. Martino, J. *et al.* The human Shu complex functions with PDS5B and
1007 SPIDR to promote homologous recombination. *Nucleic Acids Res* **47**,
1008 10151-10165 (2019).
1009 21. Lu, C.H. *et al.* Swi5-Sfr1 stimulates Rad51 recombinase filament assembly
1010 by modulating Rad51 dissociation. *Proc Natl Acad Sci U S A* **115**, E10059-
1011 E10068 (2018).
1012 22. Tanaka, K., Kagawa, W., Kinebuchi, T., Kurumizaka, H. & Miyagawa, K.
1013 Human Rad54B is a double-stranded DNA-dependent ATPase and has
1014 biochemical properties different from its structural homolog in yeast,
1015 Tid1/Rdh54. *Nucleic Acids Res* **30**, 1346-1353 (2002).
1016 23. Zhang, Z., Fan, H.Y., Goldman, J.A. & Kingston, R.E. Homology-driven
1017 chromatin remodeling by human RAD54. *Nat Struct Mol Biol* **14**, 397-405
1018 (2007).
1019 24. Liang, F. *et al.* Promotion of RAD51-Mediated Homologous DNA Pairing
1020 by the RAD51AP1-UAF1 Complex. *Cell Rep* **15**, 2118-2126 (2016).
1021 25. Parplys, A.C. *et al.* NUCKS1 is a novel RAD51AP1 paralog important for
1022 homologous recombination and genome stability. *Nucleic Acids Res* **43**,
1023 9817-9834 (2015).
1024 26. Wiese, C. *et al.* Promotion of homologous recombination and genomic
1025 stability by RAD51AP1 via RAD51 recombinase enhancement. *Mol Cell*

1026 **28**, 482-490 (2007).
1027 27. Bugreev, D.V., Mazina, O.M. & Mazin, A.V. Bloom syndrome helicase
1028 stimulates RAD51 DNA strand exchange activity through a novel
1029 mechanism. *J Biol Chem* **284**, 26349-26359 (2009).
1030 28. Bugreev, D.V., Yu, X., Egelman, E.H. & Mazin, A.V. Novel pro- and anti-
1031 recombination activities of the Bloom's syndrome helicase. *Genes Dev* **21**,
1032 3085-3094 (2007).
1033 29. Xue, C. *et al.* Single-molecule visualization of human BLM helicase as it
1034 acts upon double- and single-stranded DNA substrates. *Nucleic Acids Res*
1035 **47**, 11225-11237 (2019).
1036 30. Sommers, J.A. *et al.* FANCJ uses its motor ATPase to destabilize protein-
1037 DNA complexes, unwind triplexes, and inhibit RAD51 strand exchange. *J*
1038 *Biol Chem* **284**, 7505-7517 (2009).
1039 31. Schwendener, S. *et al.* Physical interaction of RECQ5 helicase with
1040 RAD51 facilitates its anti-recombinase activity. *J Biol Chem* **285**, 15739-
1041 15745 (2010).
1042 32. Xue, C. *et al.* Single-molecule visualization of human RECQ5 interactions
1043 with single-stranded DNA recombination intermediates. *Nucleic Acids Res*
1044 **49**, 285-305 (2021).
1045 33. Chu, W.K. *et al.* FBH1 influences DNA replication fork stability and
1046 homologous recombination through ubiquitylation of RAD51. *Nat Commun*
1047 **6**, 5931 (2015).
1048 34. Simandlova, J. *et al.* FBH1 helicase disrupts RAD51 filaments in vitro and
1049 modulates homologous recombination in mammalian cells. *J Biol Chem*
1050 **288**, 34168-34180 (2013).
1051 35. Moldovan, G.L. *et al.* Inhibition of homologous recombination by the
1052 PCNA-interacting protein PARI. *Mol Cell* **45**, 75-86 (2012).
1053 36. Adolph, M.B. *et al.* RADX controls RAD51 filament dynamics to regulate
1054 replication fork stability. *Mol Cell* **81**, 1074-1083 e1075 (2021).
1055 37. Dungrawala, H. *et al.* RADX Promotes Genome Stability and Modulates
1056 Chemosensitivity by Regulating RAD51 at Replication Forks. *Mol Cell* **67**,
1057 374-386 e375 (2017).
1058 38. Croteau, D.L., Popuri, V., Opresko, P.L. & Bohr, V.A. Human RecQ
1059 helicases in DNA repair, recombination, and replication. *Annu Rev*
1060 *Biochem* **83**, 519-552 (2014).
1061 39. Scully, R., Panday, A., Elango, R. & Willis, N.A. DNA double-strand break

repair-pathway choice in somatic mammalian cells. *Nat Rev Mol Cell Biol* **20**, 698-714 (2019).

40. Grey, C. & de Massy, B. Chromosome Organization in Early Meiotic Prophase. *Front Cell Dev Biol* **9**, 688878 (2021).
41. Ito, M. & Shinohara, A. Chromosome architecture and homologous recombination in meiosis. *Front Cell Dev Biol* **10**, 1097446 (2022).
42. Yadav, V.K. & Claeys Bouuaert, C. Mechanism and Control of Meiotic DNA Double-Strand Break Formation in S. cerevisiae. *Front Cell Dev Biol* **9**, 642737 (2021).
43. Bishop, D.K., Park, D., Xu, L. & Kleckner, N. DMC1: a meiosis-specific yeast homolog of E. coli recA required for recombination, synaptonemal complex formation, and cell cycle progression. *Cell* **69**, 439-456 (1992).
44. Brown, M.S. & Bishop, D.K. DNA strand exchange and RecA homologs in meiosis. *Cold Spring Harb Perspect Biol* **7**, a016659 (2014).
45. Crickard, J.B. & Greene, E.C. The biochemistry of early meiotic recombination intermediates. *Cell Cycle* **17**, 2520-2530 (2018).
46. Deans, B., Griffin, C.S., Maconochie, M. & Thacker, J. Xrcc2 is required for genetic stability, embryonic neurogenesis and viability in mice. *EMBO J* **19**, 6675-6685 (2000).
47. Kuznetsov, S.G., Haines, D.C., Martin, B.K. & Sharan, S.K. Loss of Rad51c leads to embryonic lethality and modulation of Trp53-dependent tumorigenesis in mice. *Cancer Res* **69**, 863-872 (2009).
48. Lim, D.S. & Hasty, P. A mutation in mouse rad51 results in an early embryonic lethal that is suppressed by a mutation in p53. *Mol Cell Biol* **16**, 7133-7143 (1996).
49. Pittman, D.L. & Schimenti, J.C. Midgestation lethality in mice deficient for the RecA-related gene, Rad51d/Rad51l3. *Genesis* **26**, 167-173 (2000).
50. Prakash, R. *et al.* XRCC3 loss leads to midgestational embryonic lethality in mice. *DNA Repair (Amst)* **108**, 103227 (2021).
51. Shu, Z., Smith, S., Wang, L., Rice, M.C. & Kmiec, E.B. Disruption of muREC2/RAD51L1 in mice results in early embryonic lethality which can Be partially rescued in a p53(-/-) background. *Mol Cell Biol* **19**, 8686-8693 (1999).
52. Tsuzuki, T. *et al.* Targeted disruption of the Rad51 gene leads to lethality in embryonic mice. *Proc Natl Acad Sci U S A* **93**, 6236-6240 (1996).
53. Matsuzaki, K., Kondo, S., Ishikawa, T. & Shinohara, A. Human RAD51

1098 paralogue SWSAP1 fosters RAD51 filament by regulating the anti-
1099 recombinase FIGNL1 AAA+ ATPase. *Nat Commun* **10**, 1407 (2019).
1100 54. Prakash, R. *et al.* Distinct pathways of homologous recombination
1101 controlled by the SWS1-SWSAP1-SPIDR complex. *Nat Commun* **12**, 4255
1102 (2021).
1103 55. Shang, Y. *et al.* MEIOK21: a new component of meiotic recombination
1104 bridges required for spermatogenesis. *Nucleic Acids Res* **48**, 6624-6639
1105 (2020).
1106 56. Takemoto, K. *et al.* Meiosis-Specific C19orf57/4930432K21Rik/BRME1
1107 Modulates Localization of RAD51 and DMC1 to DSBs in Mouse Meiotic
1108 Recombination. *Cell Rep* **31**, 107686 (2020).
1109 57. Zhang, J., Fujiwara, Y., Yamamoto, S. & Shibuya, H. A meiosis-specific
1110 BRCA2 binding protein recruits recombinases to DNA double-strand
1111 breaks to ensure homologous recombination. *Nat Commun* **10**, 722 (2019).
1112 58. Zhang, J. *et al.* The BRCA2-MEILB2-BRME1 complex governs meiotic
1113 recombination and impairs the mitotic BRCA2-RAD51 function in cancer
1114 cells. *Nat Commun* **11**, 2055 (2020).
1115 59. Chester, N., Kuo, F., Kozak, C., O'Hara, C.D. & Leder, P. Stage-specific
1116 apoptosis, developmental delay, and embryonic lethality in mice
1117 homozygous for a targeted disruption in the murine Bloom's syndrome
1118 gene. *Genes Dev* **12**, 3382-3393 (1998).
1119 60. Wesoly, J. *et al.* Differential contributions of mammalian Rad54 paralogs
1120 to recombination, DNA damage repair, and meiosis. *Mol Cell Biol* **26**, 976-
1121 989 (2006).
1122 61. McNally, F.J. & Roll-Mecak, A. Microtubule-severing enzymes: From
1123 cellular functions to molecular mechanism. *J Cell Biol* **217**, 4057-4069
1124 (2018).
1125 62. Yuan, J. & Chen, J. FIGNL1-containing protein complex is required for
1126 efficient homologous recombination repair. *Proc Natl Acad Sci U S A* **110**,
1127 10640-10645 (2013).
1128 63. Fernandes, J.B. *et al.* FIGL1 and its novel partner FLIP form a conserved
1129 complex that regulates homologous recombination. *PLoS Genet* **14**,
1130 e1007317 (2018).
1131 64. Girard, C. *et al.* AAA-ATPase FIDGETIN-LIKE 1 and Helicase FANCM
1132 Antagonize Meiotic Crossovers by Distinct Mechanisms. *PLoS Genet* **11**,
1133 e1005369 (2015).

1134 65. Hu, Q. *et al.* Meiotic Chromosome Association 1 Interacts with TOP3alpha
1135 and Regulates Meiotic Recombination in Rice. *Plant Cell* **29**, 1697-1708
1136 (2017).
1137 66. Yang, S. *et al.* FIGNL1 Inhibits Non-homologous Chromosome
1138 Association and Crossover Formation. *Front Plant Sci* **13**, 945893 (2022).
1139 67. Kumar, R., Duhamel, M., Coutant, E., Ben-Nahia, E. & Mercier, R.
1140 Antagonism between BRCA2 and FIGL1 regulates homologous
1141 recombination. *Nucleic Acids Res* **47**, 5170-5180 (2019).
1142 68. Sharan, S.K. *et al.* Embryonic lethality and radiation hypersensitivity
1143 mediated by Rad51 in mice lacking Brca2. *Nature* **386**, 804-810 (1997).
1144 69. Sadate-Ngatchou, P.I., Payne, C.J., Dearth, A.T. & Braun, R.E. Cre
1145 recombinase activity specific to postnatal, premeiotic male germ cells in
1146 transgenic mice. *Genesis* **46**, 738-742 (2008).
1147 70. Yuan, L., Brundell, E. & Hoog, C. Expression of the meiosis-specific
1148 synaptonemal complex protein 1 in a heterologous system results in the
1149 formation of large protein structures. *Exp Cell Res* **229**, 272-275 (1996).
1150 71. Yuan, L. *et al.* The murine SCP3 gene is required for synaptonemal
1151 complex assembly, chromosome synapsis, and male fertility. *Mol Cell* **5**,
1152 73-83 (2000).
1153 72. Yuan, L. *et al.* The synaptonemal complex protein SCP3 can form
1154 multistranded, cross-striated fibers in vivo. *J Cell Biol* **142**, 331-339 (1998).
1155 73. Mahadevaiah, S.K. *et al.* Recombinational DNA double-strand breaks in
1156 mice precede synapsis. *Nat Genet* **27**, 271-276 (2001).
1157 74. Luo, M. *et al.* MEIOB exhibits single-stranded DNA-binding and
1158 exonuclease activities and is essential for meiotic recombination. *Nat*
1159 *Commun* **4**, 2788 (2013).
1160 75. Souquet, B. *et al.* MEIOB targets single-strand DNA and is necessary for
1161 meiotic recombination. *PLoS Genet* **9**, e1003784 (2013).
1162 76. Yoshida, K. *et al.* The mouse RecA-like gene Dmc1 is required for
1163 homologous chromosome synapsis during meiosis. *Mol Cell* **1**, 707-718
1164 (1998).
1165 77. Ashley, T. *et al.* Dynamic changes in Rad51 distribution on chromatin
1166 during meiosis in male and female vertebrates. *Chromosoma* **104**, 19-28
1167 (1995).
1168 78. Ikeya, T., Shinohara, A., Sato, S., Tabata, S. & Ogawa, T. Localization of
1169 mouse Rad51 and Lim15 proteins on meiotic chromosomes at late stages

1170 of prophase 1. *Genes Cells* **1**, 379-389 (1996).
1171 79. Tarsounas, M., Morita, T., Pearlman, R.E. & Moens, P.B. RAD51 and
1172 DMC1 form mixed complexes associated with mouse meiotic
1173 chromosome cores and synaptonemal complexes. *J Cell Biol* **147**, 207-
1174 220 (1999).
1175 80. Shi, B. *et al.* Dual functions for the ssDNA-binding protein RPA in meiotic
1176 recombination. *PLoS Genet* **15**, e1007952 (2019).
1177 81. Moens, P.B. *et al.* The time course and chromosomal localization of
1178 recombination-related proteins at meiosis in the mouse are compatible
1179 with models that can resolve the early DNA-DNA interactions without
1180 reciprocal recombination. *J Cell Sci* **115**, 1611-1622 (2002).
1181 82. Baker, S.M. *et al.* Involvement of mouse Mlh1 in DNA mismatch repair and
1182 meiotic crossing over. *Nat Genet* **13**, 336-342 (1996).
1183 83. Baudat, F., Manova, K., Yuen, J.P., Jasin, M. & Keeney, S. Chromosome
1184 synapsis defects and sexually dimorphic meiotic progression in mice
1185 lacking Spo11. *Mol Cell* **6**, 989-998 (2000).
1186 84. Romanienko, P.J. & Camerini-Otero, R.D. The mouse Spo11 gene is
1187 required for meiotic chromosome synapsis. *Mol Cell* **6**, 975-987 (2000).
1188 85. Hinch, A.G. *et al.* The Configuration of RPA, RAD51, and DMC1 Binding
1189 in Meiosis Reveals the Nature of Critical Recombination Intermediates.
1190 *Mol Cell* **79**, 689-701 e610 (2020).
1191 86. Khil, P.P., Smagulova, F., Brick, K.M., Camerini-Otero, R.D. & Petukhova,
1192 G.V. Sensitive mapping of recombination hotspots using sequencing-
1193 based detection of ssDNA. *Genome Res* **22**, 957-965 (2012).
1194 87. Smagulova, F. *et al.* Genome-wide analysis reveals novel molecular
1195 features of mouse recombination hotspots. *Nature* **472**, 375-378 (2011).
1196 88. Altmannova, V. *et al.* The role of bivalent ions in the regulation of D-loop
1197 extension mediated by DMC1 during meiotic recombination. *iScience* **25**,
1198 105439 (2022).
1199 89. Li, X. & Heyer, W.D. RAD54 controls access to the invading 3'-OH end
1200 after RAD51-mediated DNA strand invasion in homologous recombination
1201 in Saccharomyces cerevisiae. *Nucleic Acids Res* **37**, 638-646 (2009).
1202 90. Li, X., Stith, C.M., Burgers, P.M. & Heyer, W.D. PCNA is required for
1203 initiation of recombination-associated DNA synthesis by DNA polymerase
1204 delta. *Mol Cell* **36**, 704-713 (2009).
1205 91. Bugreev, D.V. *et al.* The resistance of DMC1 D-loops to dissociation may

1206 account for the DMC1 requirement in meiosis. *Nat Struct Mol Biol* **18**, 56-
1207 60 (2011).
1208 92. Finsterbusch, F. *et al.* Alignment of Homologous Chromosomes and
1209 Effective Repair of Programmed DNA Double-Strand Breaks during
1210 Mouse Meiosis Require the Minichromosome Maintenance Domain
1211 Containing 2 (MCMDC2) Protein. *PLoS Genet* **12**, e1006393 (2016).
1212 93. Her, C., Wu, X., Bailey, S.M. & Doggett, N.A. Mouse MutS homolog 4 is
1213 predominantly expressed in testis and interacts with MutS homolog 5.
1214 *Mamm Genome* **12**, 73-76 (2001).
1215 94. Kneitz, B. *et al.* MutS homolog 4 localization to meiotic chromosomes is
1216 required for chromosome pairing during meiosis in male and female mice.
1217 *Genes Dev* **14**, 1085-1097 (2000).
1218 95. Li, X.C. & Schimenti, J.C. Mouse pachytene checkpoint 2 (trip13) is
1219 required for completing meiotic recombination but not synapsis. *PLoS*
1220 *Genet* **3**, e130 (2007).
1221 96. Lutzmann, M. *et al.* MCM8- and MCM9-deficient mice reveal
1222 gametogenesis defects and genome instability due to impaired
1223 homologous recombination. *Mol Cell* **47**, 523-534 (2012).
1224 97. McNairn, A.J., Rinaldi, V.D. & Schimenti, J.C. Repair of Meiotic DNA
1225 Breaks and Homolog Pairing in Mouse Meiosis Requires a
1226 Minichromosome Maintenance (MCM) Paralog. *Genetics* **205**, 529-537
1227 (2017).
1228 98. Roig, I. *et al.* Mouse TRIP13/PCH2 is required for recombination and
1229 normal higher-order chromosome structure during meiosis. *PLoS Genet* **6**
1230 (2010).
1231 99. Benson, F.E., Stasiak, A. & West, S.C. Purification and characterization of
1232 the human Rad51 protein, an analogue of E. coli RecA. *EMBO J* **13**, 5764-
1233 5771 (1994).
1234 100. Dupaigne, P. *et al.* Rad51 polymerization reveals a new chromatin
1235 remodeling mechanism. *PLoS One* **3**, e3643 (2008).
1236 101. North, J.A. *et al.* ATP-dependent nucleosome unwrapping catalyzed by
1237 human RAD51. *Nucleic Acids Res* **41**, 7302-7312 (2013).
1238 102. Senavirathne, G., Mahto, S.K., Hanne, J., O'Brian, D. & Fishel, R. Dynamic
1239 unwrapping of nucleosomes by HsRAD51 that includes sliding and
1240 rotational motion of histone octamers. *Nucleic Acids Res* **45**, 685-698
1241 (2017).

1242 103. Holzen, T.M., Shah, P.P., Olivares, H.A. & Bishop, D.K. Tid1/Rdh54
1243 promotes dissociation of Dmc1 from nonrecombinogenic sites on meiotic
1244 chromatin. *Genes Dev* **20**, 2593-2604 (2006).
1245 104. Shah, P.P. *et al.* Swi2/Snf2-related translocases prevent accumulation of
1246 toxic Rad51 complexes during mitotic growth. *Mol Cell* **39**, 862-872 (2010).
1247 105. Mason, J.M. *et al.* RAD54 family translocases counter genotoxic effects of
1248 RAD51 in human tumor cells. *Nucleic Acids Res* **43**, 3180-3196 (2015).
1249 106. Tokuhiro, K. *et al.* Calreticulin is required for development of the cumulus
1250 oocyte complex and female fertility. *Sci Rep* **5**, 14254 (2015).
1251 107. de Boer, E., Lhuissier, F.G. & Heyting, C. Cytological analysis of
1252 interference in mouse meiosis. *Methods Mol Biol* **558**, 355-382 (2009).
1253 108. Peters, A.H., Plug, A.W., van Vugt, M.J. & de Boer, P. A drying-down
1254 technique for the spreading of mammalian meiocytes from the male and
1255 female germline. *Chromosome Res* **5**, 66-68 (1997).
1256 109. Brick, K., Pratto, F., Sun, C.Y., Camerini-Otero, R.D. & Petukhova, G.
1257 Analysis of Meiotic Double-Strand Break Initiation in Mammals. *Methods*
1258 *Enzymol* **601**, 391-418 (2018).
1259 110. Ramirez, F. *et al.* deepTools2: a next generation web server for deep-
1260 sequencing data analysis. *Nucleic Acids Res* **44**, W160-165 (2016).
1261 111. Matsuo, Y., Sakane, I., Takizawa, Y., Takahashi, M. & Kurumizaka, H.
1262 Roles of the human Rad51 L1 and L2 loops in DNA binding. *FEBS J* **273**,
1263 3148-3159 (2006).
1264 112. Lange, J. *et al.* The Landscape of Mouse Meiotic Double-Strand Break
1265 Formation, Processing, and Repair. *Cell* **167**, 695-708 e616 (2016).
1266 113. Boekhout, M. *et al.* REC114 Partner ANKRD31 Controls Number, Timing,
1267 and Location of Meiotic DNA Breaks. *Mol Cell* **74**, 1053-1068 e1058 (2019).
1268
1269

1270 **Figure legends**
1271
1272 **Fig. 1. Defective spermatogenesis in *Fignl1* cKO mice.**
1273 (a) Scheme of mouse *Fignl1 flox* and *Δ* alleles. Yellow and blue boxes and black
1274 triangles represent untranslated regions (UTRs), coding sequence (CDS), and
1275 *loxP* sequences, respectively.
1276 (b) Representative image of testes in *Fignl1*$^{+/+}$ *Stra8-Cre*$^{+}$ (left) and *Fignl1*$^{flox/\Delta}$
1277 *Stra8-Cre*$^{+}$ (right) mice.
1278 (c) Testis weights of mice with different combinations of genotypes. Adult testes
1279 (9-20 weeks) were analyzed. The red bars are means.
1280 (d) Immunoblotting of FIGNL1 from whole-testis extracts of mice with different
1281 genotypes. α-tubulin is a loading control.
1282 (e) Sperm numbers in *Fignl1*$^{+/+}$ *Stra8-Cre*$^{+}$ (black circles) and *Fignl1*$^{flox/\Delta}$ *Stra8-*
1283 *Cre*$^{+}$ (blue open circles) mice. Sperms from adult Cauda epididymis (11-17
1284 weeks) were counted. The red bars are means.
1285 (f) Representative images of seminiferous tubule sections from the testis of
1286 *Fignl1*$^{+/+}$ *Stra8-Cre*$^{+}$ (Ctrl) and *Fignl1*$^{flox/\Delta}$ *Stra8-Cre*$^{+}$ (*Fignl1* cKO) mice. The
1287 sections were stained with hematoxylin and eosin (H&E). Sg, spermatogonia; Sc
1288 (L), leptotene spermatocytes; Sc (P), pachytene spermatocytes; St, spermatids.
1289 (g) Distribution of different meiotic prophase I stages in Ctrl (gray bars) and *Fignl1*
1290 cKO (blue open bars). >100 cells were counted from each animal. The red bars
1291 are SDs from three animals of each genotype.
1292 (h) Distribution of FIGNL1-positive and -negative cells at different meiotic
1293 prophase I stages in Ctrl (gray bars) and *Fignl1* cKO (blue open bars). Squashed
1294 testicular cells were immunostained for FIGNL1, γH2AX, and SYCP3. >100
1295 leptotene/zygotene cells (with pan-nuclear γH2AX staining) and
1296 pachytene/diplotene cells (with the sex body-specific γH2AX staining) were
1297 analyzed from each animal. The means of two mice of each genotype are
1298 indicated. Lept., leptonema; Zyg., zygonema; Pach., pachynema; dipl.,
1299 diplonema. Representative images of testicular cell squashes are shown in
1300 Extended Data Fig. 1.
1301 (i) Representative images of spermatocyte chromosome spreads immunostained
1302 for SYCP1 (green) and SYCP3 (magenta) at zygonema in Ctrl and *Fignl1* cKO.
1303 Bottom panels are magnified images of regions with yellow dotted rectangles.
1304 (j) Quantification of the frequency of synapsis defects in Ctrl (gray bars) and
1305 *Fignl1* cKO (blue open bars). >90 cells were analyzed from each animal. The red

1306 bars are SDs from three mice of each genotype.
1307 In (f)-(i), genotypes of indicated animals are Ctrl, *Fignl1*$^{+/+}$ *Stra8-Cre*$^{+}$; *Fignl1* cKO,
1308 *Fignl1*$^{flox/\Delta}$ *Stra8-Cre*$^{+}$. The results of unpaired *t*-tests are indicated in the graphs:
1309 ****$p \leq 0.0001$.
1310 Scale bars, 50 μm in (f) and 10 μm for whole-nucleus images and 2 μm for
1311 magnified images in (i).
1312
1313 **Fig. 2. Accumulation of RAD51 and DMC1 in meiotic prophase I in *Fignl1***
1314 **cKO spermatocytes.**
1315 (a) Representative images of spermatocyte chromosome spreads
1316 immunostained for DMC1 (white in the top panels and green in the bottom panels)
1317 and SYCP3 (magenta) at indicated meiotic prophase I stages in Ctrl and *Fignl1*
1318 cKO.
1319 (b) Quantification of DMC1 focus numbers at different meiotic prophase I stages
1320 in Ctrl (black circles) and *Fignl1* cKO (blue open circles). The red bars are means.
1321 (c) Representative images of spermatocyte chromosome spreads
1322 immunostained for RAD51 (white in the top panels and green in the bottom
1323 panels) and SYCP3 (magenta) at indicated meiotic prophase I stages in Ctrl and
1324 *Fignl1* cKO.
1325 (d) Quantification of RAD51 focus numbers at different meiotic prophase I stages
1326 in Ctrl (black circles) and *Fignl1* cKO (blue open circles). The red bars are means.
1327 (e) Quantification of focus numbers of RAD51 (green), DMC1 (magenta) and
1328 RAD51-DMC1 colocalization (brown) at different meiotic prophase I stages in Ctrl
1329 (filled circles) and *Fignl1* cKO (open circles). The black bars are means.
1330 Representative images of spermatocyte chromosome spreads are shown in
1331 Extended Data Fig. 4.
1332 (f) Quantification of the frequency of RAD51-DMC1 colocalization at different
1333 meiotic prophase I stages in Ctrl (filled circles) and *Fignl1* cKO (open circles). The
1334 degrees of RAD51 foci colocalizing with DMC1 (left, green) and DMC1 foci
1335 colocalizing with RAD51 (right, magenta) are shown. The black bars are means.
1336 Genotypes of indicated animals are Ctrl, *Fignl1*$^{+/+}$ *Stra8-Cre*$^{+}$; *Fignl1* cKO,
1337 *Fignl1*$^{flox/\Delta}$ *Stra8-Cre*$^{+}$. The results of the Mann-Whitney *U*-test are indicated in
1338 the graphs: ****$p \leq 0.0001$. The total number of cells analyzed is indicated below
1339 the graphs.
1340 Scale bars in (a) and (c), 10 μm. Prelept., preleptonema; lept., leptonema; zyg.,
1341 zygonema.

1342

1343 **Fig. 3. Deregulated meiotic recombination in *Fignl1* cKO spermatocytes.**

1344 (a) Representative images of spermatocyte chromosome spreads
1345 immunostained for RPA2 (white in the top panels and green in the bottom panels)
1346 and SYCP3 (magenta) at indicated meiotic prophase I stages in Ctrl and *Fignl1*
1347 cKO.

1348 (b) Quantification of RPA2 focus numbers at different meiotic prophase I stages
1349 in Ctrl (black circles) and *Fignl1* cKO (blue open circles). The red bars are means.

1350 (c) Representative images of spermatocyte chromosome spreads
1351 immunostained for MSH4 (white in the left panels and green in the right panels),
1352 SYCP1 (magenta) and SYCP3 (blue) at mid zygonema in Ctrl and *Fignl1* cKO.
1353 Bottom panels are magnified images of regions with dotted yellow.

1354 (d) Quantification of MSH4 focus numbers at mid zygonema in Ctrl (black circles)
1355 and *Fignl1* cKO (blue open circles). The red bars are means.

1356 (e) The correlation between MSH4 focus number and total SC length at mid
1357 zygonema in Ctrl (black circles) and *Fignl1* cKO (blue open circles). Pearson's *r*
1358 is shown in parentheses. A black solid line and a blue dashed line indicate linear
1359 regression for Ctrl and *Fignl1* cKO, respectively.

1360 (f) Quantification of MSH4 focus density on the SCs at mid-zygonema in Ctrl
1361 (black circles) and *Fignl1* cKO (blue open circles). The red bars are means. In (e)
1362 and (f), mid zygotene nuclei with 40-120 μm of total SC length per nucleus were
1363 analyzed.

1364 Genotypes of indicated animals are: Ctrl, *Fignl1*$^{+/+}$ *Stra8-Cre*$^{+}$; *Fignl1* cKO,
1365 *Fignl1*$^{flox/\Delta}$ *Stra8-Cre*$^{+}$. The results of the Mann-Whitney *U*-test are indicated in
1366 the graphs: ****$p \leq 0.0001$. The total number of cells analyzed is indicated below
1367 the graphs.

1368 Scale bars in (a) and (c), 10 μm and 2 μm for magnified images in (c).

1369

1370 **Fig. 4. Accumulation of RAD51 and DMC1 in pre-leptotene *Fignl1* cKO**
1371 **spermatocytes.**

1372 (a) Representative images of spermatocyte chromosome spreads
1373 immunostained for RAD51 (left), SYCP3 (middle) and EdU (right) at
1374 preleptonema in Ctrl and *Fignl1* cKO.

1375 (b) Quantification of RAD51 focus numbers at preleptonema in Ctrl (black circles)
1376 and *Fignl1* cKO (blue open circles). The red solid bars and dashed bars are
1377 means for total cells and RAD51-positive cells (with >10 RAD51 foci; 26/38 and

1378 25/48 cells in early and mid/late preleptonema, respectively), respectively.
1379 (c) Representative images of spermatocyte chromosome spreads
1380 immunostained for DMC1 (left), SYCP3 (middle), and EdU (right) at
1381 preleptonema in Ctrl and *Fignl1* cKO.
1382 (d) Quantification of DMC1 focus numbers at preleptonema in Ctrl (black circles)
1383 and *Fignl1* cKO (blue open circles). The red solid bars and dashed bars are
1384 means for total cells and DMC1-positive cells (with >30 DMC1 foci; 28/39 and
1385 26/45 cells in early and mid/late preleptonema, respectively), respectively.
1386 Genotypes of indicated animals are Ctrl, *Fignl1*$^{+/+}$ *Stra8-Cre*$^{+}$; *Fignl1* cKO,
1387 *Fignl1*$^{flox/\Delta}$ *Stra8-Cre*$^{+}$. The results of the Mann-Whitney *U*-test are indicated in
1388 the graphs: ****$p \leq 0.0001$. The total numbers of cells analyzed are indicated
1389 below the graphs.
1390 Scale bars in (a) and (c), 10 μm.
1391
1392 **Fig. 5. SPO11-independent accumulation of RAD51 and DMC1 in *Fignl1* cKO**
1393 **spermatocytes.**
1394 (a) Representative images of spermatocyte chromosome spreads
1395 immunostained for RAD51 (white in the top panels and green in the bottom
1396 panels) and SYCP3 (magenta) at leptonema in *Spo11* KO, *Fignl1* cKO and *Spo11*
1397 KO *Fignl1* cKO.
1398 (b) Quantification of RAD51 focus numbers at different meiotic prophase I stages
1399 in *Spo11* KO (orange circles), *Fignl1* cKO (blue open circles), and *Spo11* KO
1400 *Fignl1* cKO (purple open circles). The red bars are means. Cells in which Stra8-
1401 Cre recombinase seemed to fail excision of the *Fignl1*$^{\Delta}$ allele in *Spo11* KO *Fignl1*
1402 cKO (<30 RAD51 foci) are excluded. Quantification including these cells is shown
1403 in Extended Data Fig. 5a.
1404 (c) Representative images of spermatocyte chromosome spreads
1405 immunostained for DMC1 (white in the top panels and green in the bottom panels)
1406 and SYCP3 (magenta) at early zygonema in *Spo11* KO, *Fignl1* cKO and *Spo11*
1407 KO *Fignl1* cKO.
1408 (d) Quantification of DMC1 focus numbers at different meiotic prophase I stages
1409 in *Spo11* KO (orange circles), *Fignl1* cKO (blue open circles) and *Spo11* KO
1410 *Fignl1* cKO (purple open circles). The red bars are means. Cells in which Stra8-
1411 Cre recombinase seemed to fail excision of the *Fignl1*$^{\Delta}$ allele in *Spo11* KO *Fignl1*
1412 cKO (<60 DMC1 foci) are excluded. Quantification including these cells is shown
1413 in Extended Data Fig. 5b.

1414 (e) Representative images of spermatocyte chromosome spreads
1415 immunostained for RAD51 (green), DMC1 (magenta) and SYCP3 (blue) at late
1416 zygonema/early leptonema in *Spo11* KO *Fignl1* cKO. The bottom panels are
1417 magnified images of regions with yellow dotted rectangles.
1418 (f) Quantification of focus numbers of RAD51 (green open circles), DMC1
1419 (magenta open circles), and RAD51-DMC1 colocalization (brawn open circles) at
1420 different meiotic prophase I stages in *Spo11* KO *Fignl1* cKO. The black bars are
1421 means.
1422 (g) Quantification of the frequency of RAD51-DMC1 colocalization at different
1423 meiotic prophase I stages in *Spo11* KO *Fignl1* cKO. The degrees of RAD51 foci
1424 colocalizing with DMC1 (left, green open circles) and DMC1 foci colocalizing with
1425 RAD51 (right, magenta open circles) are shown. The black bars are means.
1426 Genotypes of indicated animals are: *Spo11* KO, *Spo11*$^{-/-}$ *Fignl1*$^{flox/\Delta}$; *Fignl1* cKO,
1427 *Fignl1*$^{flox/\Delta}$ *Stra8-Cre*$^{+}$; *Spo11* KO *Fignl1* cKO, *Spo11*$^{-/-}$ *Fignl1*$^{flox/\Delta}$ *Stra8-Cre*$^{+}$. The
1428 results of the Mann-Whitney *U*-test are indicated in the graphs: ****$p \leq 0.0001$.
1429 The total number of cells analyzed is indicated below the graphs.
1430 Scale bars in (a), (c) and (e), 10 μm and 2 μm for magnified images in (e). Prelept.,
1431 preleptonema; lept., leptonema; zyg., zygonema.
1432
1433 **Fig. 6. Persistent RAD51 binding at recombination sites in *Fignl1* cKO**
1434 **spermatocytes.**
1435 (a) RAD51 ChIP-SSDS signals (green) in Ctrl and *Fignl1* cKO with Spo11-oligo
1436 counts (blue) and DMC1 ChIP-SSDS signals (black) in wild-type at an indicated
1437 chromosomal region with a hotspot on mouse chromosome 2.
1438 (b) The heatmap of RAD51 ChIP-SSDS signals (green) in Ctrl and *Fignl1* cKO
1439 and Spo11-oligo counts (blue) and DMC1 ChIP-SSDS signals (black) in wild-type.
1440 The 4,000 most active meiotic recombination hotspots on autosomes identified
1441 by Spo11-oligo in wild-type are ordered by SPO11-oligos counts [112]. ChIP-SSDS
1442 signals are centered relative to hotspot centers. In (a) and (b), Spo11-oligo and
1443 DMC1 ChIP-SSDS data are from previous studies [112, 113].
1444 (c) Representative images of spermatocyte chromosome spreads
1445 immunostained for RAD51 (green), RPA2 (magenta) and SYCP3 (blue) at mid
1446 zygonema in Ctrl and *Fignl1* cKO. Bottom panels are magnified images of regions
1447 with yellow dotted rectangles. Scale bars, 10 μm for whole-nucleus images and
1448 2 μm for magnified images.
1449 (d) Quantification of focus numbers of RAD51 (green), RPA2 (magenta) and

1450 RAD51-RPA2 colocalization (brawn) at mid zygonema in Ctrl (filled circles) and
1451 *Fignl1* cKO (open circles). The black bars are means.
1452 (e) Quantification of the frequency of RAD51-RPA2 colocalization at mid-
1453 zygonema in Ctrl (black circles) and *Fignl1* cKO (blue open circles). The degree
1454 of RPA2 foci colocalizing with RAD51 is shown. The red bars are means.
1455 Genotypes of indicated animals are: Ctrl, *Fignl1*$^{+/+}$ *Stra8-Cre*$^{+}$; *Fignl1* cKO,
1456 *Fignl1*$^{flox/\Delta}$ *Stra8-Cre*$^{+}$. The results of the Mann-Whitney *U*-test are indicated: ****$p$
1457 ≤ 0.0001. The total numbers of cells analyzed are indicated below the graphs.
1458
1459 **Fig. 7. *Fignl1* deficiency rescues defects in RAD51 and DMC1 assembly**
1460 **caused by *Swsap1* deficiency.**
1461 (a) Representative images of spermatocyte chromosome spreads
1462 immunostained for RAD51 (white in the top panels and green in the bottom
1463 panels) and SYCP3 (magenta) at early zygonema in Ctrl, *Swsap1* KO, *Fignl1*
1464 cKO and *Swsap1* KO *Fignl1* cKO.
1465 (b) Quantification of RAD51 focus numbers at different meiotic prophase I stages
1466 in Ctrl (black circles), *Swsap1* KO (orange circles), *Fignl1* cKO (blue open circles)
1467 and *Swsap1* KO *Fignl1* cKO (purple open circles). The red bars are means.
1468 (c) Representative images of spermatocyte chromosome spreads
1469 immunostained for DMC1 (white in the top panels and green in the bottom panels)
1470 and SYCP3 (magenta) at early zygonema in Ctrl, *Swsap1* KO, *Fignl1* cKO, and
1471 *Swsap1* KO *Fignl1* cKO.
1472 (d) Quantification of DMC1 focus numbers at different meiotic prophase I stages
1473 in Ctrl (black circles), *Swsap1* KO (orange circles), *Fignl1* cKO (blue open circles),
1474 and *Swsap1* KO *Fignl1* cKO (purple open circles). The red bars are means.
1475 Genotypes of indicated animals are *Swsap1* KO, *Swsap1*$^{-/-}$ *Fignl1*$^{flox/\Delta}$; *Fignl1*
1476 cKO, *Fignl1*$^{flox/\Delta}$ *Stra8-Cre*$^{+}$; *Swsap1* KO *Fignl1* cKO, *Swsap1*$^{-/-}$ *Fignl1*$^{flox/\Delta}$ *Stra8-*
1477 *Cre*$^{+}$. The results of the Mann-Whitney *U*-test are indicated in the graphs: ****$p$ ≤
1478 0.0001. The total numbers of cells analyzed are indicated below the graphs.
1479 Scale bars in (a) and (c), 10 μm.
1480
1481 **Fig. 8. FIGNL1 disrupts RAD51-DNA complexes.**
1482 (a) Electrophoresis mobility shift assay showing *in vitro* disruption of RAD51-DNA
1483 complexes by FIGNL1. A representative gel image among triplicate is shown.
1484 Human RAD51 protein was incubated with either Cy5-labelled ssDNA (40nt) or
1485 dsDNA (40bp) in the presence of ATP. After the formation of the protein-DNA

1486 complex, purified human FINGL1ΔN was added at the indicated concentration
1487 and further incubated. The complexes were analyzed by polyacrylamide gel
1488 electrophoresis and the fluorescence from the DNAs was captured.
1489 (b) Quantification of free ssDNA or dsDNA in (A). The red bars are means and
1490 SDs from three independent experiments.
1491 (c) Model of FIGNL1 function in spermatocytes. In meiotic S-phase and early
1492 meiotic prophase I, FIGNL1 dissociates RAD51 and DMC1 from dsDNAs. At
1493 meiotic DSB sites, FIGNL1 removes RAD51 and DMC1 from ssDNAs, which
1494 facilitates efficient loading of MutSγ (MSH4-MSH5) and further processing of
1495 homologous recombination to crossover outcome.
1496
1497 **Extended Data Figures:**
1498 **Extended Data Fig. 1. Depletion of FIGNL1 from early meiotic prophase I**
1499 **spermatocytes, related to Fig. 1.**
1500 Representative images of testicular cell squashes immunostained for FIGNL1
1501 (green), γH2AX (blue) and SYCP3 (magenta) in Ctrl (*Fignl1*$^{+/+}$ *Stra8-Cre*$^{+}$) and
1502 *Fignl1* cKO (*Fignl1*$^{flox/\Delta}$ *Stra8-Cre*$^{+}$). SYCP3-positive prophase I spermatocytes
1503 were categorized into two by γH2AX staining: leptotene/zygotene cells (L/Z) and
1504 pachytene/diplotene cells (P/D) show pan-nuclear γH2AX staining and the sex
1505 body-specific γH2AX staining, respectively. Scale bars, 10 μm.
1506
1507 **Extended Data Fig. 2. Deregulated meiotic recombination in *Fignl1* cKO**
1508 **spermatocytes, related to Fig. 3.**
1509 (a) Representative images of spermatocyte chromosome spreads
1510 immunostained for γH2AX (white in the top panels and green in the bottom
1511 panels) and SYCP3 (magenta) at indicated meiotic prophase I stages in Ctrl and
1512 *Fignl1* cKO.
1513 (b) Quantification of γH2AX intensity at different meiotic prophase I stages in Ctrl
1514 (black circles) and *Fignl1* cKO (blue open circles). Two independent experiments
1515 showed reduced (left; pooled results from two animals of each genotype) and one
1516 experiment showed similar (right) levels of γH2AX intensity in *Fignl1* cKO
1517 spermatocytes compared to Ctrl. The red bars are means. The results of the
1518 Mann-Whitney *U*-tests are indicated: ****$p \leq 0.0001$. The total numbers of cells
1519 analyzed are indicated below the graphs.
1520 (c) Representative images of spermatocyte chromosome spreads
1521 immunostained for MLH1 (white in the top panels and green in the bottom panels),

1522 SYCP1 (magenta), and SYCP3 (blue) at late pachynema in Ctrl and late
1523 zygonema (pachynema-like) in *Fignl1* cKO. The right panels are magnified
1524 images of regions with yellow dotted rectangles.
1525 Genotypes of indicated animals are Ctrl, *Fignl1*$^{+/+}$ *Stra8-Cre*$^{+}$; *Fignl1* cKO,
1526 *Fignl1*$^{flox/\Delta}$ *Stra8-Cre*$^{+}$.
1527 Scale bars in (a) and (c), 10 μm and 2 μm for magnified images in (c).
1528
1529 **Extended Data Fig. 3. Infrequent localization of RAD51 at ongoing**
1530 **replication fork in preleptotene *Fignl1* spermatocytes, related to Fig. 4.**
1531 (a) Representative images of spermatocyte chromosome spreads
1532 immunostained for IdU (green), RAD51 (magenta), and SYCP3 at early
1533 preleptonema in *Fignl1* cKO. The bottom panels are magnified images of regions
1534 with yellow dotted rectangles. Scale bars, 10 μm for whole-nucleus images and
1535 2 μm for magnified images.
1536 (b) Quantification of focus numbers of IdU (green open circles), RAD51 (magenta
1537 open circles), and IdU-RAD51 colocalization (brawn open circles) at early
1538 preleptonema in *Fignl1* cKO. The black bars are means.
1539 (c) Quantification of the frequency of IdU-RAD51 colocalization at early
1540 preleptonema in *Fignl1* cKO. The degrees of IdU foci colocalizing with RAD51
1541 (left, green open circles) and RAD51 foci colocalizing with IdU (right, magenta
1542 open circles) are shown. The black bars are means. The colocalization frequency
1543 was measured with and without rotating the IdU image 90$^{o}$ clockwise relative to
1544 the RAD51 image. The results of the Mann-Whitney *U*-tests are indicated.
1545 The Genotype of *Fignl1* cKO animals is *Fignl1*$^{flox/\Delta}$ *Stra8-Cre*$^{+}$.
1546
1547 **Extended Data Fig. 4. Uncoupled loading of RAD51 and DMC1 in *Fignl1* cKO**
1548 **spermatocytes, related to Fig. 2 and 4.**
1549 Representative images of spermatocyte chromosome spreads immunostained
1550 for RAD51 (green), DMC1 (magenta), and SYCP3 (blue) at indicated meiotic
1551 prophase I stages in Ctrl (*Fignl1*$^{+/+}$ *Stra8-Cre*$^{+}$) and *Fignl1* cKO (*Fignl1*$^{flox/\Delta}$ *Stra8-*
1552 *Cre*$^{+}$). The bottom panels are magnified images of regions with yellow dotted
1553 rectangles. Scale bars, 10 μm for whole-nucleus images and 2 μm for magnified
1554 images.
1555
1556 **Extended Data Fig. 5. Accumulation of RAD51 and DMC1 with low levels of**
1557 **γH2AX in *Spo11* KO *Fignl1* cKO spermatocytes, related to Fig. 5.**

1558 (a) Quantification of RAD51 focus numbers at different meiotic prophase I stages
1559 in *Spo11* KO (orange circles), *Fignl1* cKO (blue open circles), and *Spo11* KO
1560 *Fignl1* cKO (purple open circles). The red bars are means.
1561 (b) Quantification of DMC1 focus numbers at different meiotic prophase I stages
1562 in *Spo11* KO (orange circles), *Fignl1* cKO (blue open circles), and *Spo11* KO
1563 *Fignl1* cKO (purple open circles). The red bars are means.
1564 (c) Representative images of spermatocyte chromosome spreads
1565 immunostained for γH2AX (green), SYCP3 (magenta), and RAD51 (white in
1566 insets) at indicated meiotic prophase I stages in *Fignl1* cKO, *Spo11* KO and
1567 *Spo11* KO *Fignl1* cKO. Scale bars, 10 μm.
1568 (d) Quantification of γH2AX intensity at different meiotic prophase I stages in
1569 *Fignl1* cKO (blue open circles), *Spo11* KO (orange circles), and *Spo11* KO *Fignl1*
1570 cKO (purple open circles). The red bars are means.
1571 Genotypes of indicated animals are: *Spo11* KO, *Spo11*$^{-/-}$ *Fignl1*$^{flox/\Delta}$; *Fignl1* cKO,
1572 *Fignl1*$^{flox/\Delta}$ *Stra8-Cre*$^{+}$; *Spo11* KO *Fignl1* cKO, *Spo11*$^{-/-}$ *Fignl1*$^{flox/\Delta}$ *Stra8-Cre*$^{+}$. The
1573 results of the Mann-Whitney *U*-test are indicated in the graphs: ****$p \leq 0.0001$.
1574 The total number of cells analyzed is indicated below the graphs.
1575
1576 **Extended Data Fig. 6. RAD51 binding at recombination sites in *Fignl1* cKO**
1577 **spermatocytes, related to Fig. 6.**
1578 (a) RAD51 ChIP-SSDS signals (green) in Ctrl and *Fignl1* cKO with Spo11-oligo
1579 counts (blue) and DMC1 ChIP-SSDS signals (black) in wild-type at an indicated
1580 chromosomal region with multiple hotspots on mouse chromosome 3.
1581 (b) The heatmap of RAD51 ChIP-SSDS signals (green) in Ctrl and *Fignl1* cKO
1582 and Spo11-oligo counts (blue) and DMC1 ChIP-SSDS signals (black) in wild-type,
1583 as shown in Fig. 6b. Three mice of each genotype were analyzed and two RAD51
1584 antibodies with different lot numbers were used for ChIP. The results of Ctrl #1
1585 and *Fignl1* cKO #1 are shown in Fig. 6a, b, Extended Data Fig. 6a.
1586 (c) Comparison of RAD51 ChIP-SSDS signals at meiotic recombination hotspots.
1587 Each spot represents the sum of RAD51 ChIP-SSDS signals around ±2,000 bp
1588 of one of the 4,000 most active meiotic recombination hotspots on autosomes
1589 (black) used for heatmap representation in Fig. 6b, Extended Data Fig. 6a and
1590 163 active hotspots on sex chromosomes (magenta) with similar Spo11-oligo
1591 counts as the 4,000 active autosomal hotspots in wild-type [112]. Pearson's *r* for
1592 autosomal hotspots is also shown.
1593 (d) Metaplots of RAD51 ChIP-SSDS signals around meiotic recombination

1594 hotspots. Smoothed RAD51 ChIP-SSDS signals in Ctrl (top) and *Fignl1* cKO
1595 (bottom) around ±2,000 bp of the 4,000 most active meiotic recombination
1596 hotspots on autosomes used for heatmap representation are shown. Three mice
1597 of each genotype were analyzed. Black, orange and blue lines represent the
1598 results of #1, #2 and #3, respectively.
1599 Genotypes of indicated animals are: Ctrl, *Fignl1*$^{+/+}$ *Stra8-Cre*$^{+}$; *Fignl1* cKO,
1600 *Fignl1*$^{flox/\Delta}$ *Stra8-Cre*$^{+}$.
1601
1602 **Source Data**
1603 Uncropped images of immunoblotting in Fig. 1d and an unprocessed image of
1604 electrophoresis mobility shift assay in Fig. 8a are provided.
1605

1606 **Supplementary information**

1607

1608 **Supplementary Table 1. Primers used for genotyping in this study**

| Primer | Sequence (5'->3') |
|---|---|
| *Fignl1* wild-type and flox allele, forward | TATCCATATTGGGTGTCTCCTGTTAC |
| *Fignl1* wild-type and flox allele, reverse | TAGCACACACACACTGGATATAACT |
| *Fignl1* deletion allele, forward | CCGAGTATCCATATTGGGTG |
| *Fignl1* deletion allele, reverse | TGTCTGCTGTAGTCATGAGG |
| *Stra8-Cre* transgenic allele, forward | CTCCAAGGGGGTAAGGTGTAGC |
| *Stra8-Cre* transgenic allele, reverse | TTCCAGGGCGCGAGTTGATAG |
| *Swsap1* wild-type allele, forward | GAGATATCGCTTTTGATTGGTC |
| *Swsap1* wild-type allele, reverse | GAATTGAGGATGGGTACTGG |
| *Swsap1* deletion allele, forward | CGGTTTCCATATGGGGATTGGTGGCGACGA |
| *Swsap1* deletion allele, reverse | TGCCTTATTTCCTGATCCAGGCTAGCTGTC |
| *Spo11* wild-type allele, forward | TGAGATACATGGAGGAAGATGG |
| *Spo11* deletion allele, forward | CTGAGCCCAGAAAGCGAAGGAA |
| *Spo11,* common reverse | ATGTTAGTCGGCACAGCAGTAG |

1623

1624 **Supplementary Table 2. Antibodies used in this study**

| Antibody | Source | Identifier | Application | Dilution |
|---|---|---|---|---|
| Rat anti-SYCP3 (Serum) | this study | N/A | IF | 1:5,000 |
| Mouse anti-SYCP3 | Abcam | ab97672 | IF | 1:750 |
| Rabbit anti-SYCP1 | Novus Biologicals | NB300-229 | IF | 1:500 |
| Mouse anti-MLH1 | BD Pharmingen | 51-1327QR | IF | 1:50 |
| Rabbit anti-MSH4 | Abcam | ab58666 | IF | 1:200 |
| Rabbit anti-RPA2 | Abcam | ab76420 | IF | 1:200 |
| Rat anti-RPA2 | Cell Signaling | 2208 | IF | 1:100 |
| Rabbit anti-DMC1 | Santa Cruz | sc-22768 | IF | 1:200 |
| Rabbit anti-RAD51 | Santa Cruz | sc-8349 | IF | 1:100 |
| Mouse anti-RAD51 | Novus Biologicals | NB100-148 | IF, ChIP | 1:100 |
| Mouse anti-BrdU | BD Biosciences | BD347580 | IF | 1:200 |
| Rabbit anti-FIGNL1 | Proteintech | 17604-1-AP | IF | 1:100 |
| | | | IB | 1:1,000 |
| Mouse anti-α tubulin | SIGMA | T6074 | IB | 1:3,000 |
| Goat anti-mouse 488 | Molecular Probes | A-11029 | IF | 1:1,000 |
| Goat anti-rabbit 488 | Molecular Probes | A-11034 | IF | 1:1,000 |

| | | | |
|---|---|---|---|
| Goat anti-rat 488 | Molecular Probes A-11006 | IF | 1:1,000 |
| Goat anti-mouse 594 | Molecular Probes A-11032 | IF | 1:1,000 |
| Goat anti-rat 594 | Molecular Probes A-11007 | IF | 1:1,000 |
| Goat anti-rabbit 647 | Molecular Probes A-21245 | IF | 1:500 |
| Goat anti-rabbit IgG-HRP | Southern Biotech 4030-05 | IB | 1:10,000 |
| Goat anti-mouse IgG-HRP | Thermo Scientific 31430 | IB | 1:10.000 |

IF, immunofluorescence; IB, immunoblotting.; ChIP, chromatin immunoprecipitation

Ito et al., Figure 1

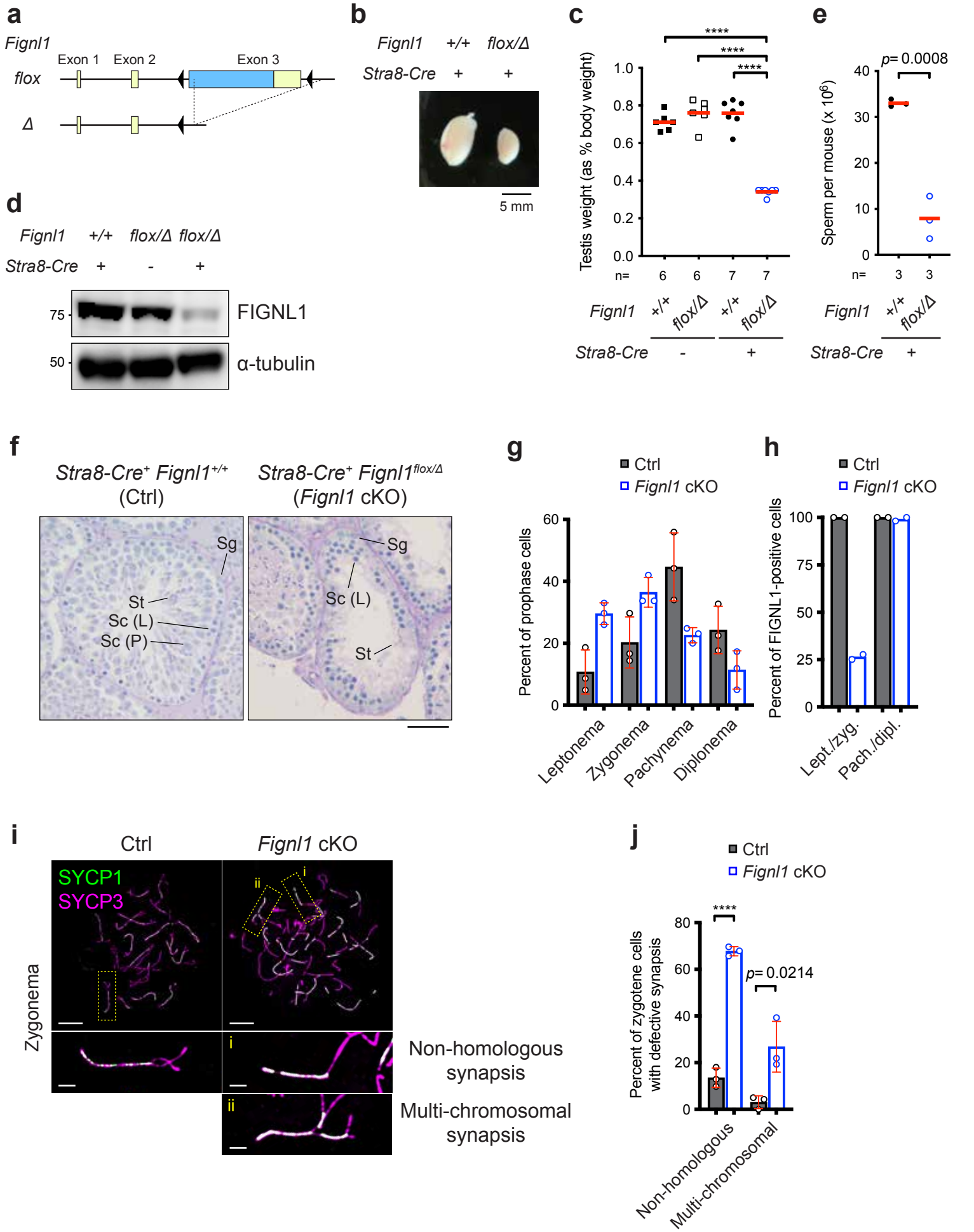

Ito et al., Figure 2

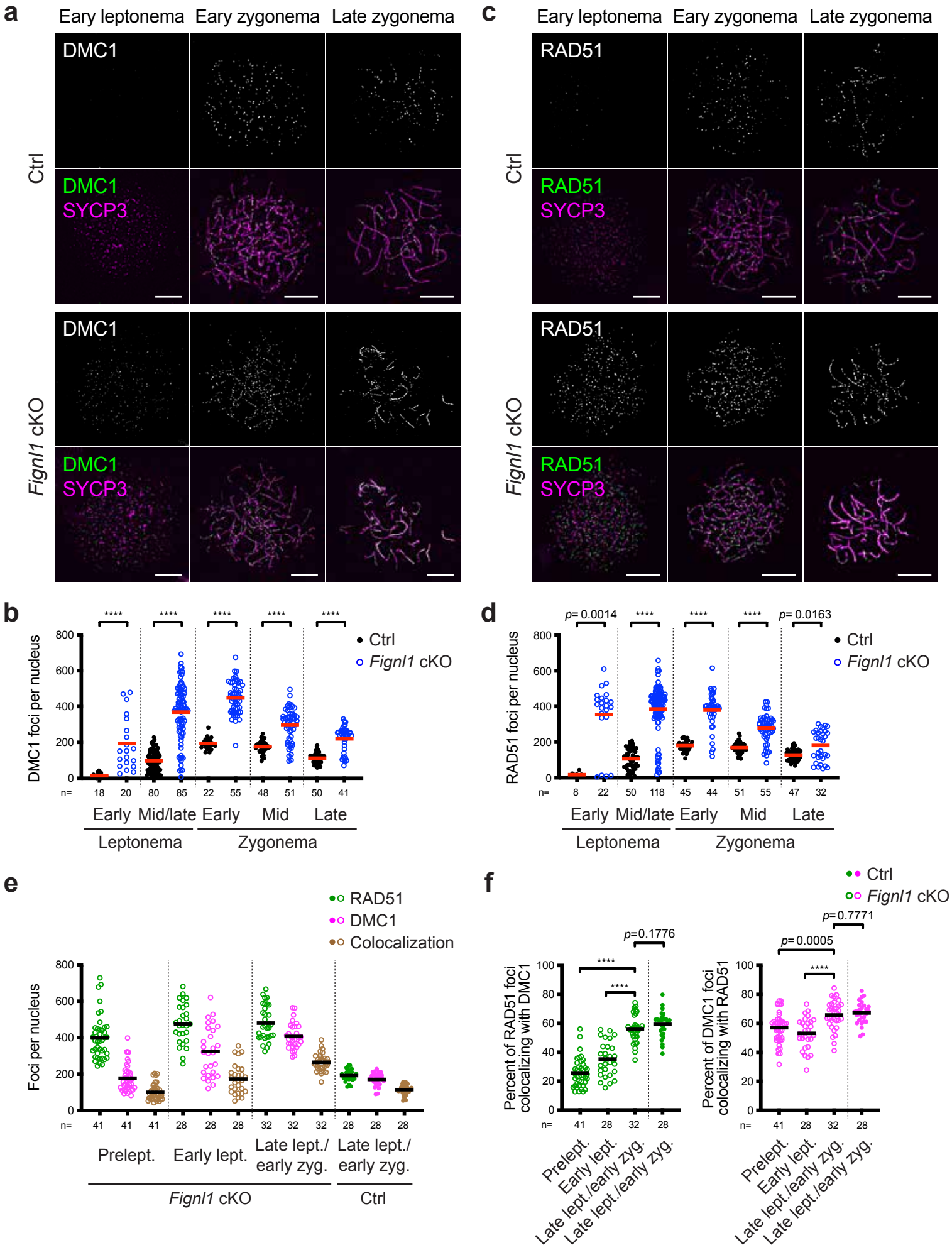

Ito et al., Figure 3

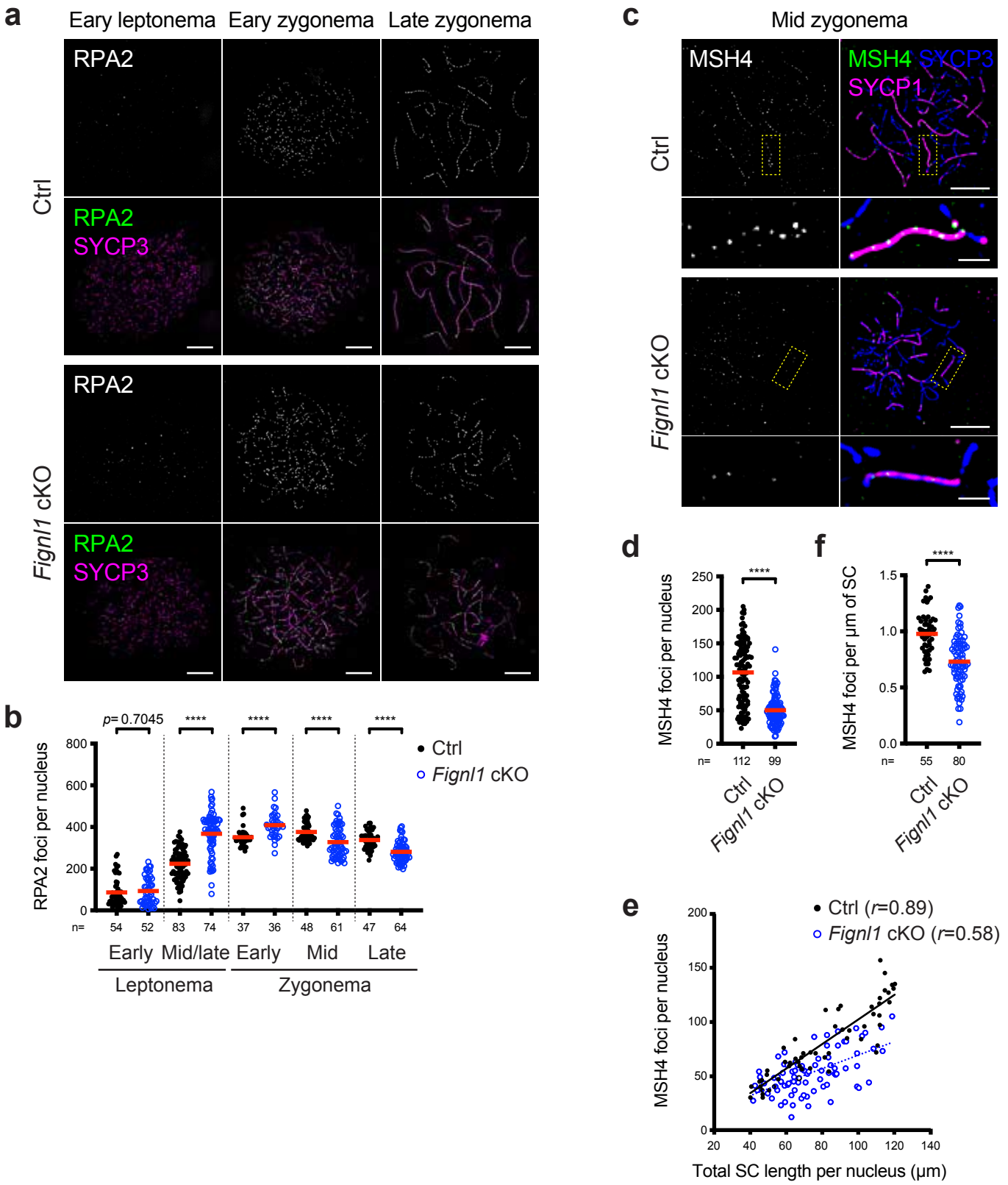

Ito et al., Figure 4

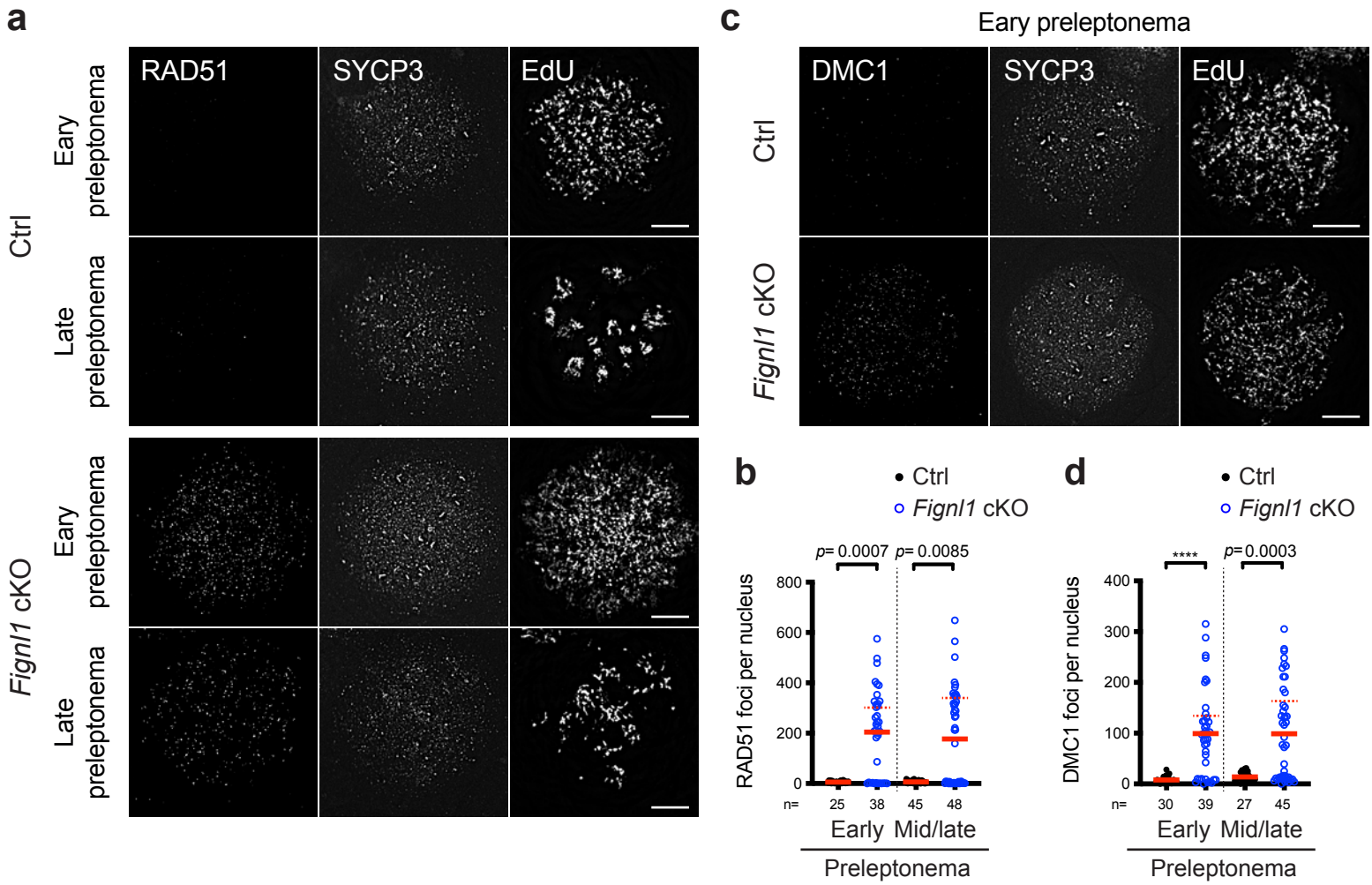

Ito et al., Figure 5

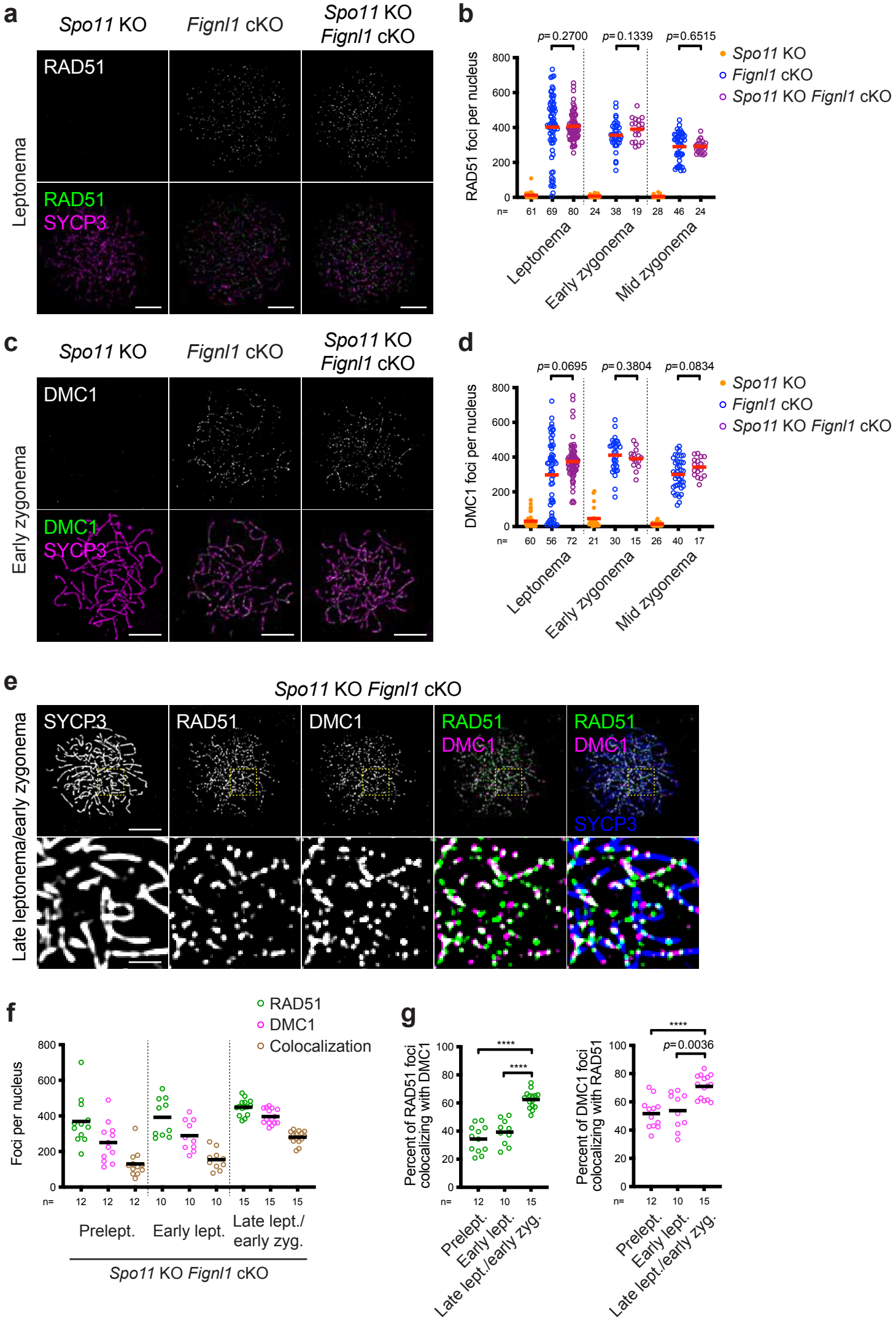

Ito et al., Figure 6

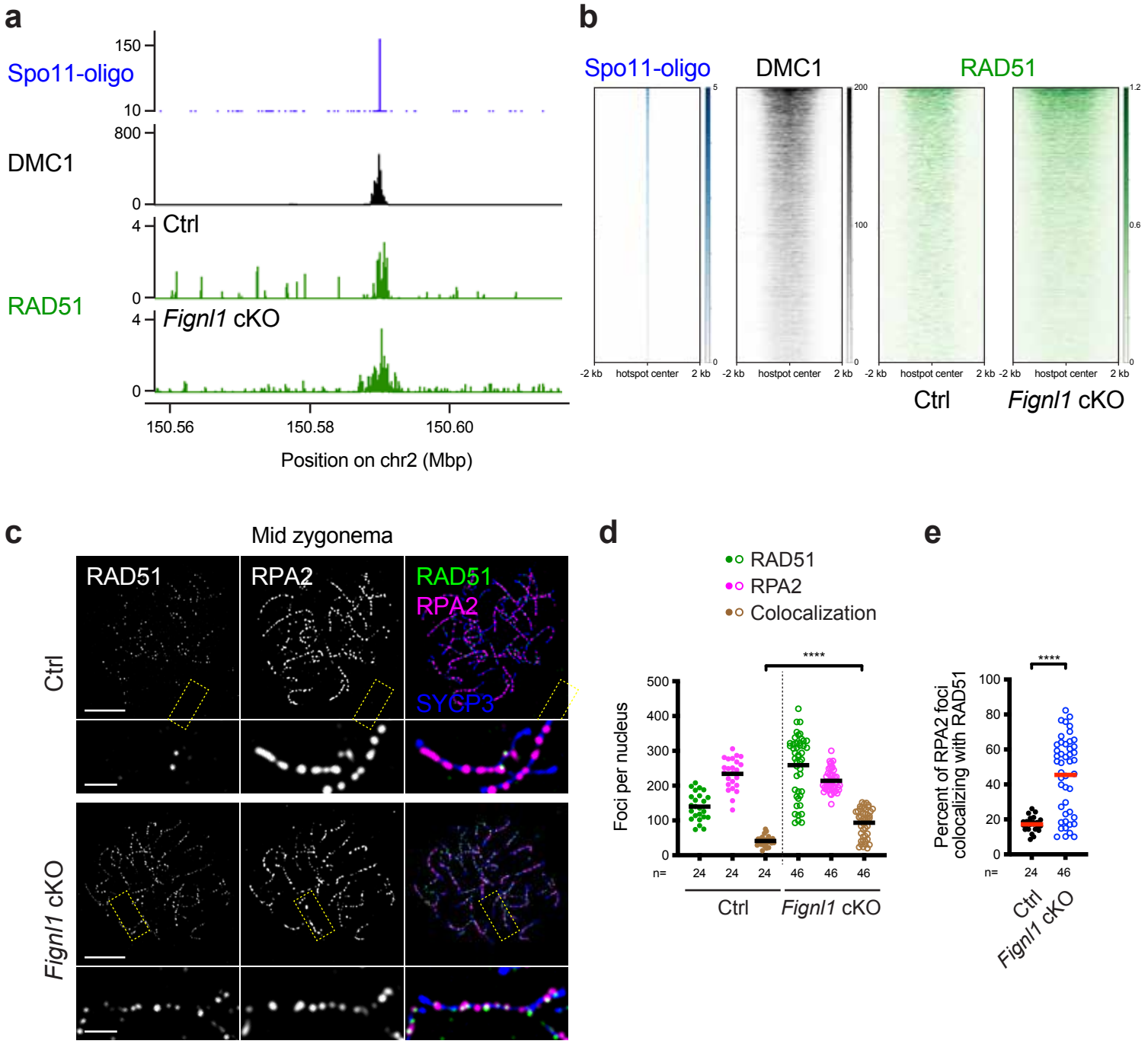

Ito et al., Figure 7

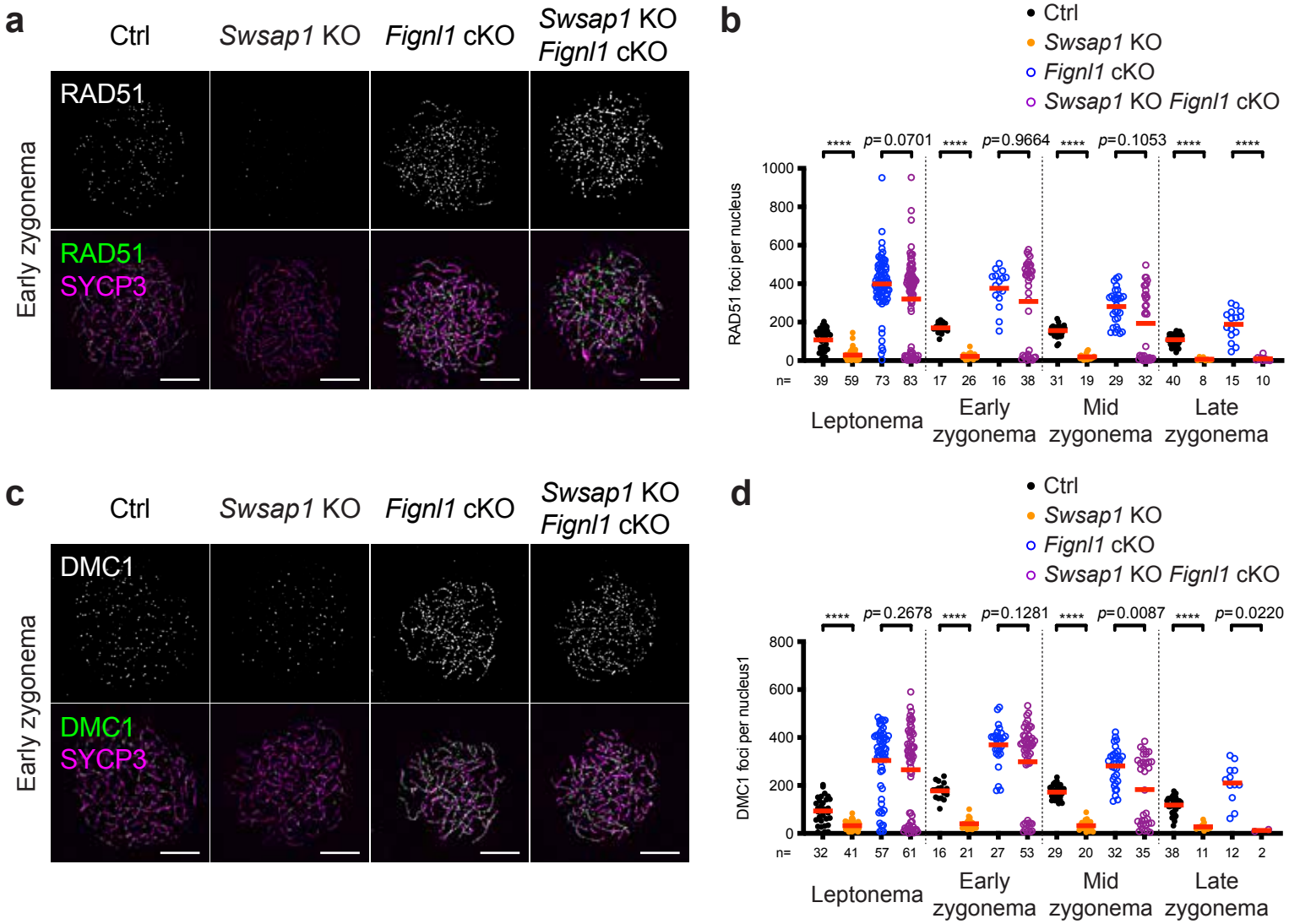

Ito et al., Figure 8

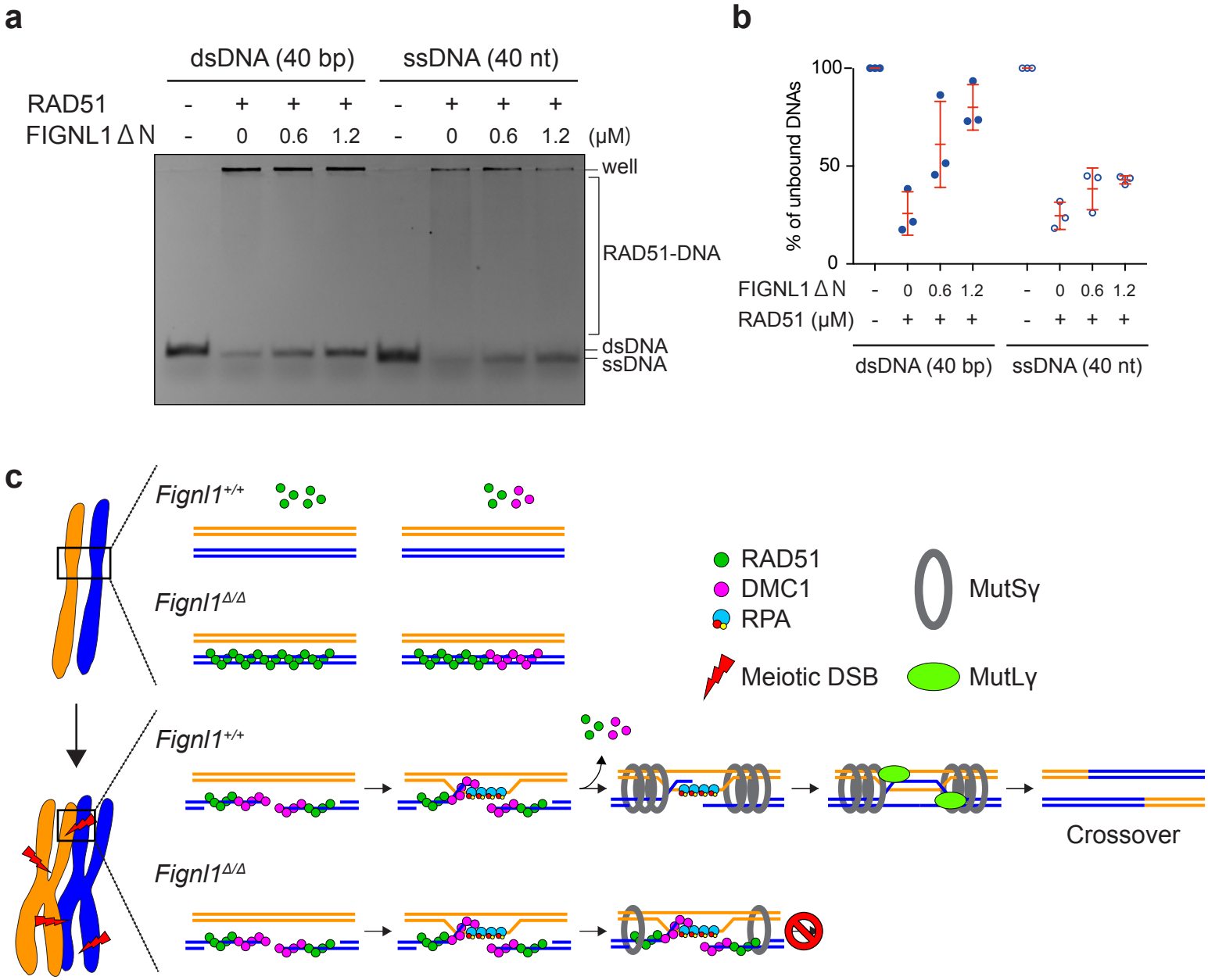

Ito et al., Extended Data Figure 1

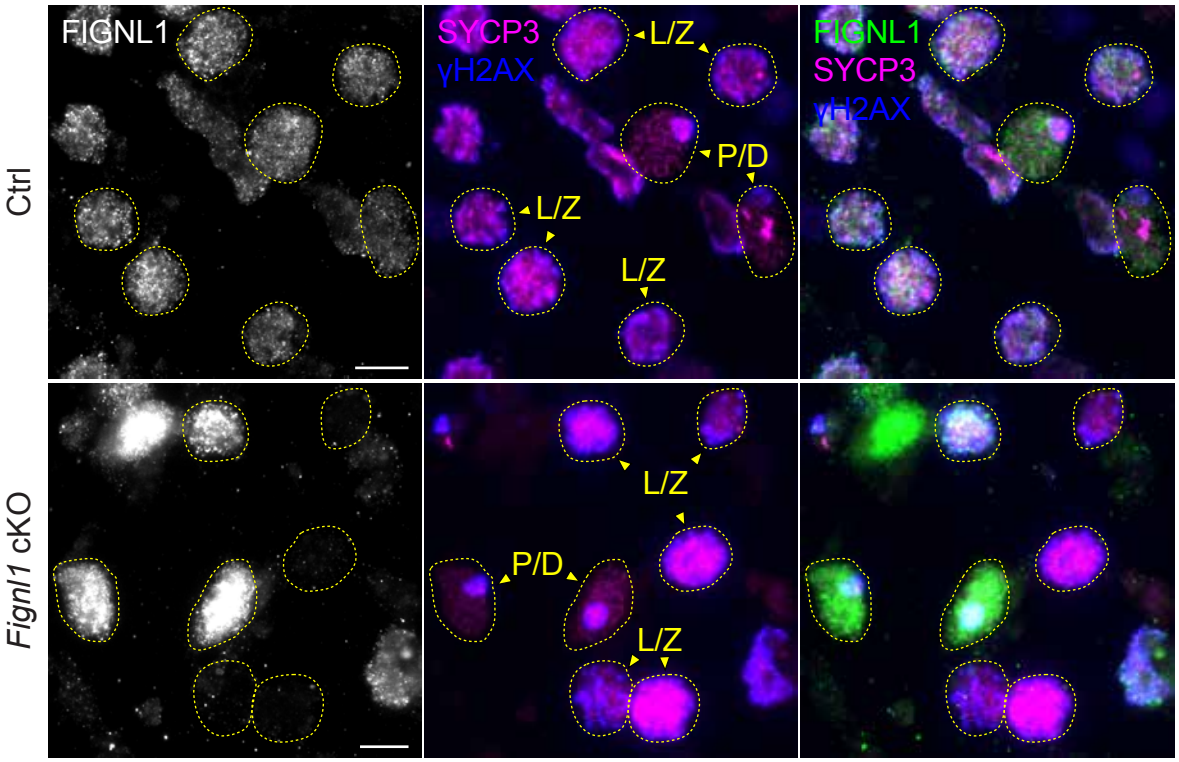

Ito et al., Extended Data Figure 2

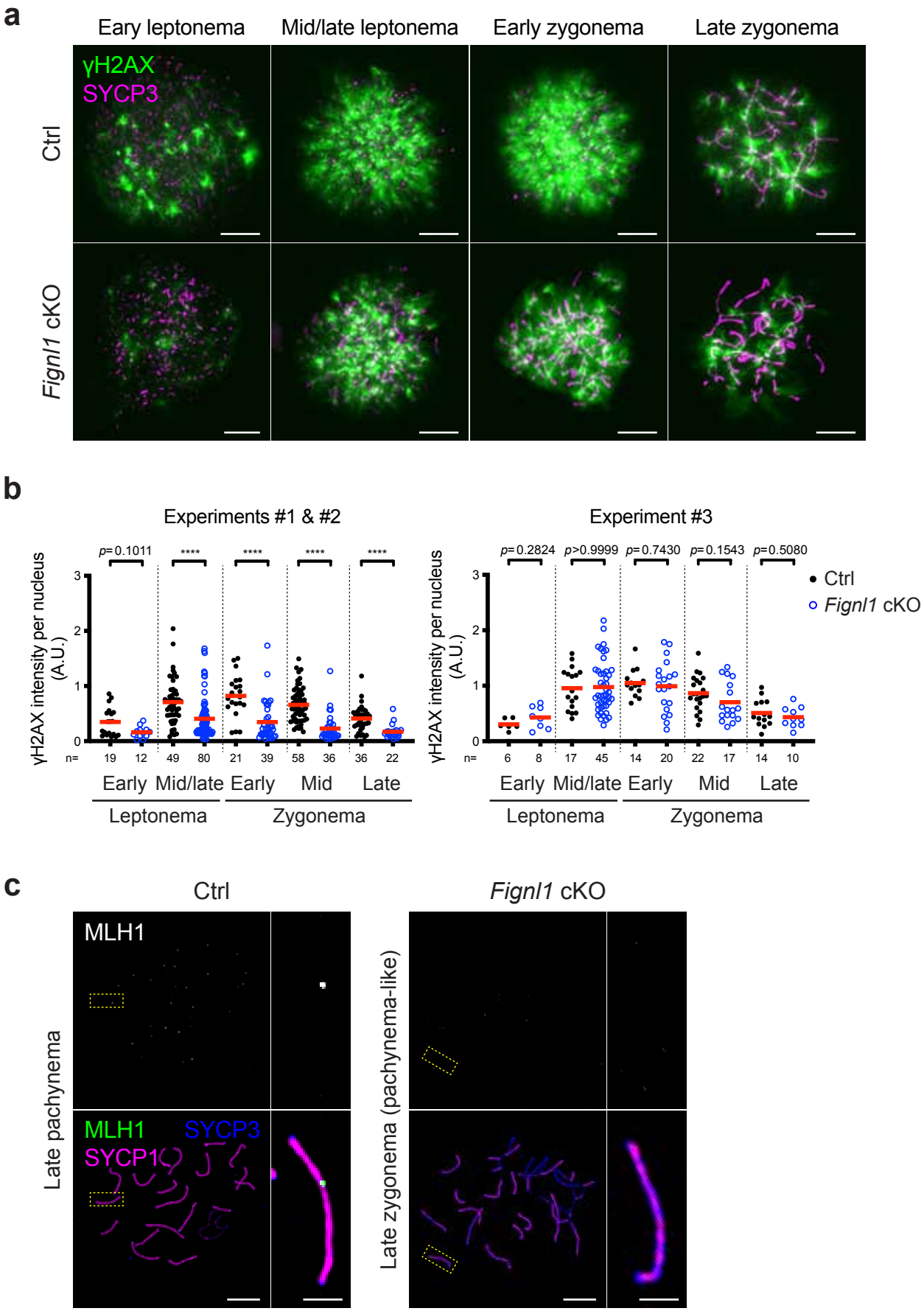

Ito et al., Extended Data Figure 3

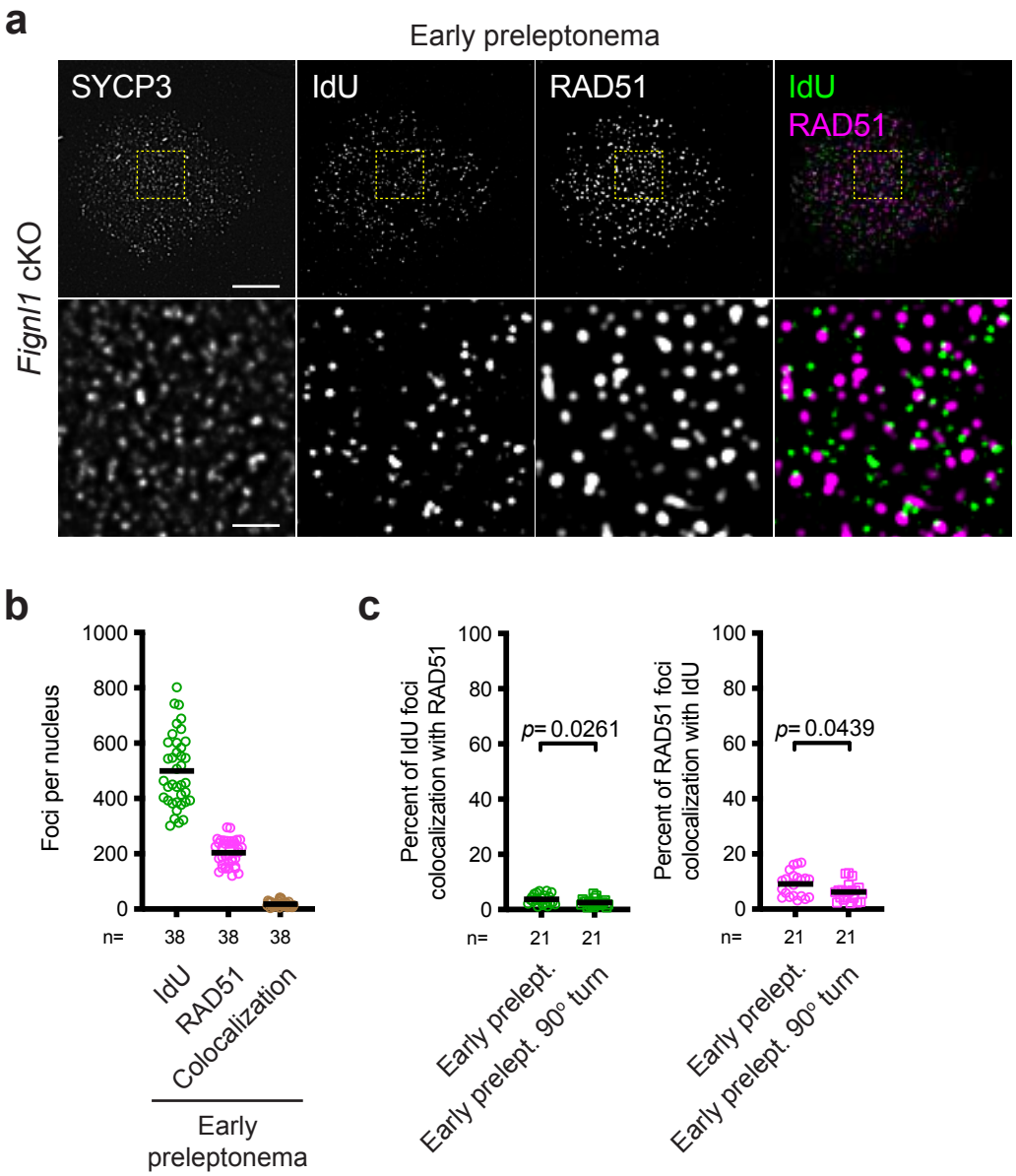

Ito et al., Extended Data Figure 4

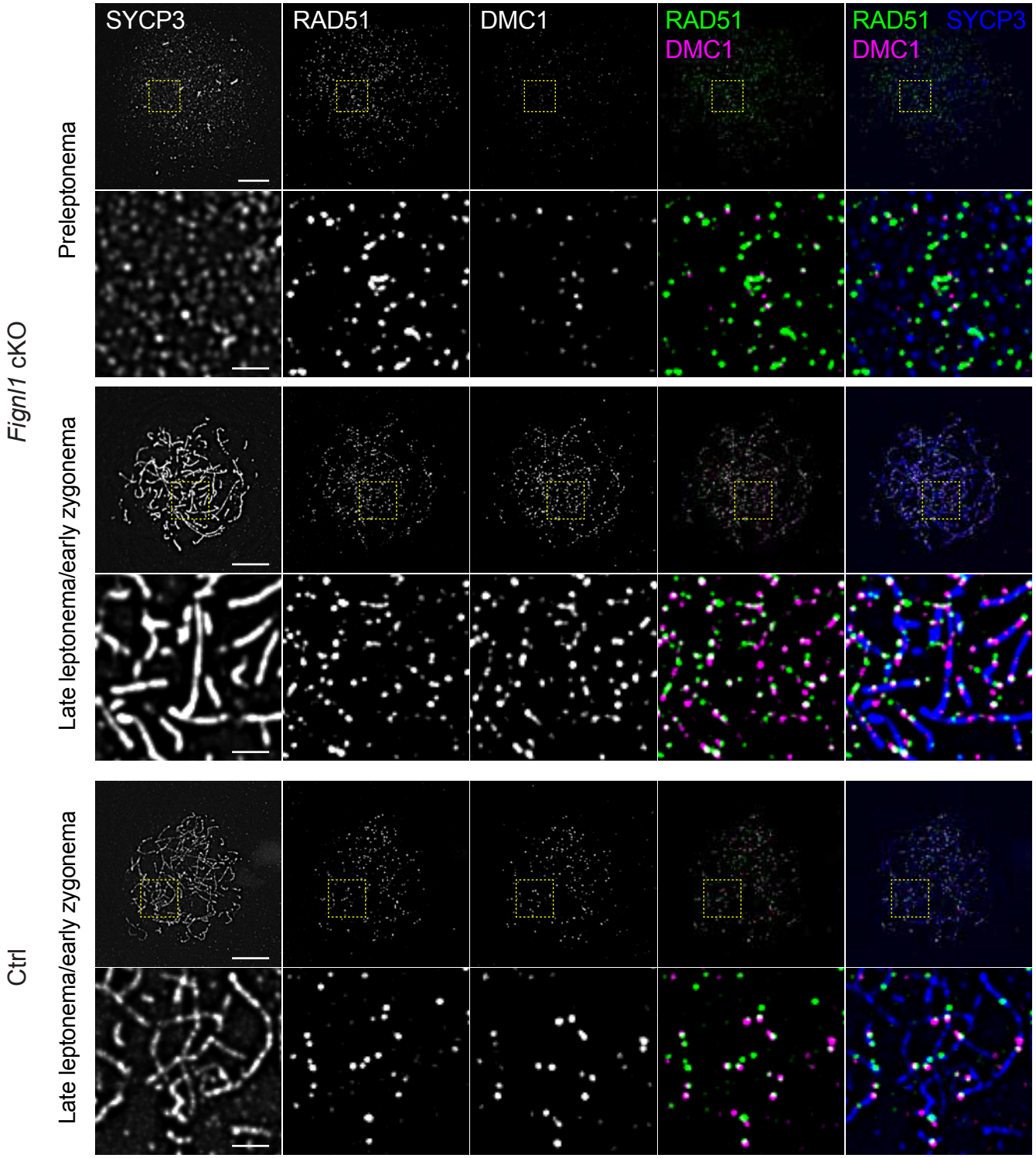

Ito et al., Extended Data Figure 5

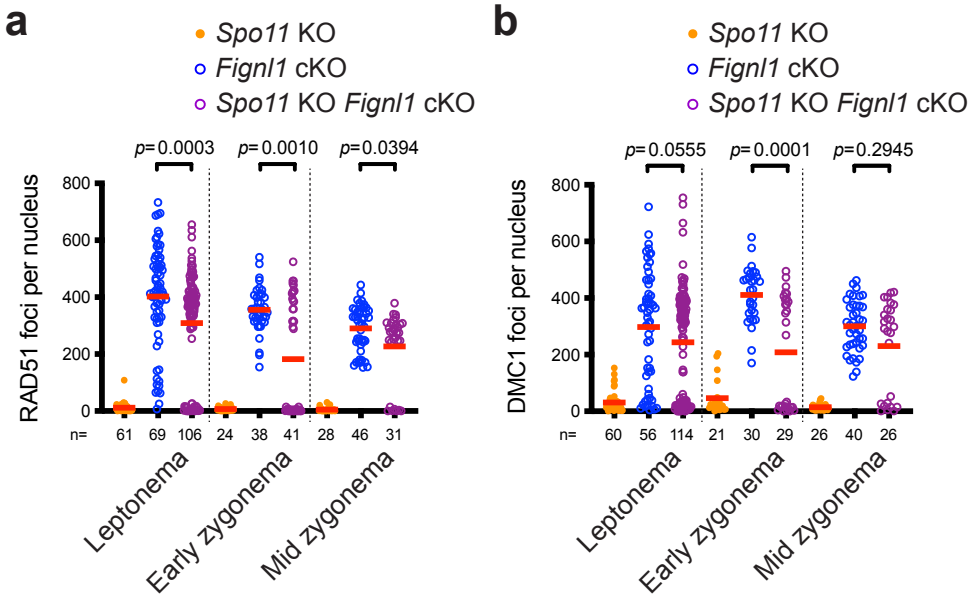


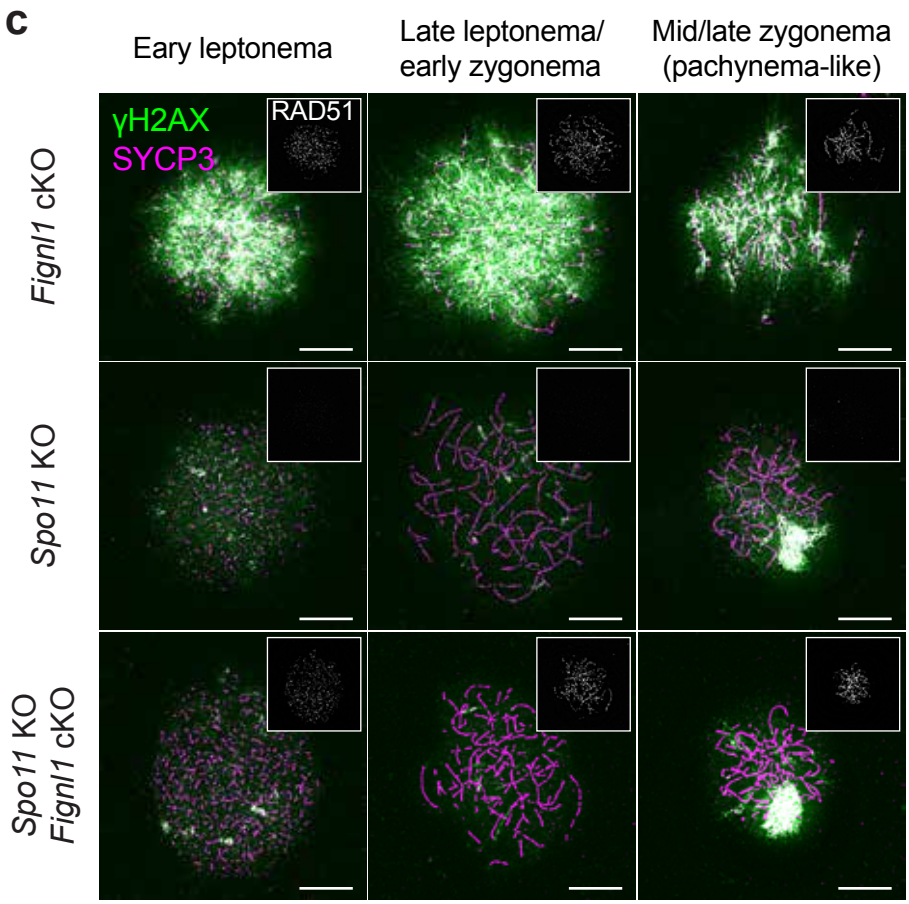


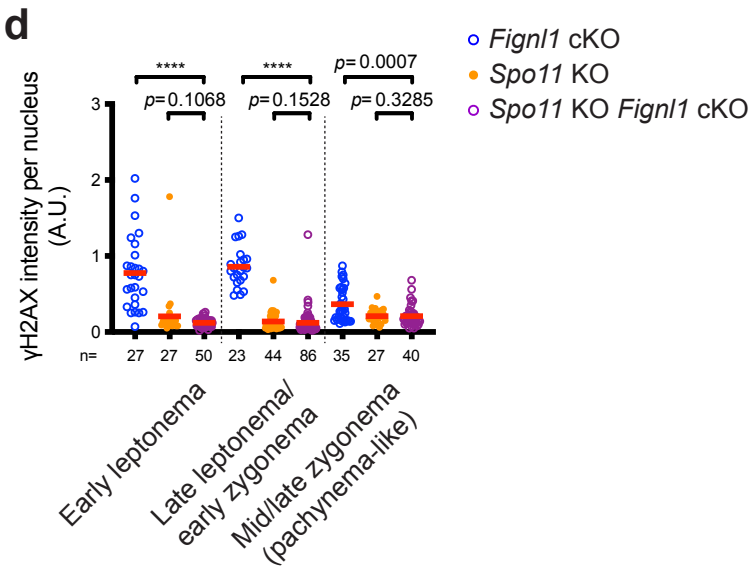

Ito et al., Extended Data Figure 6

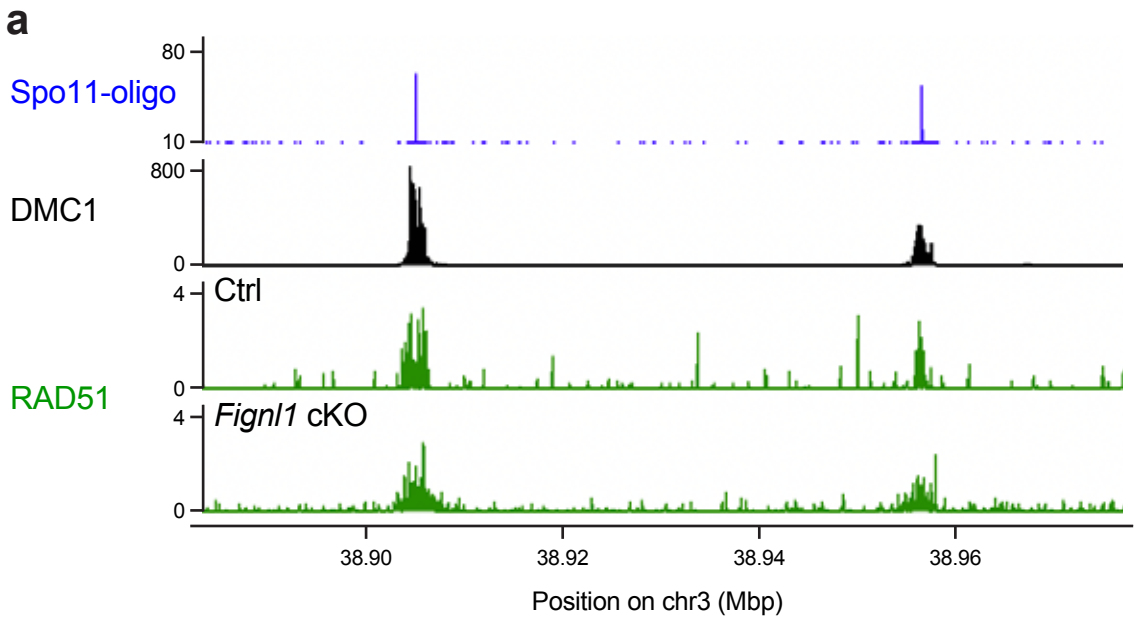


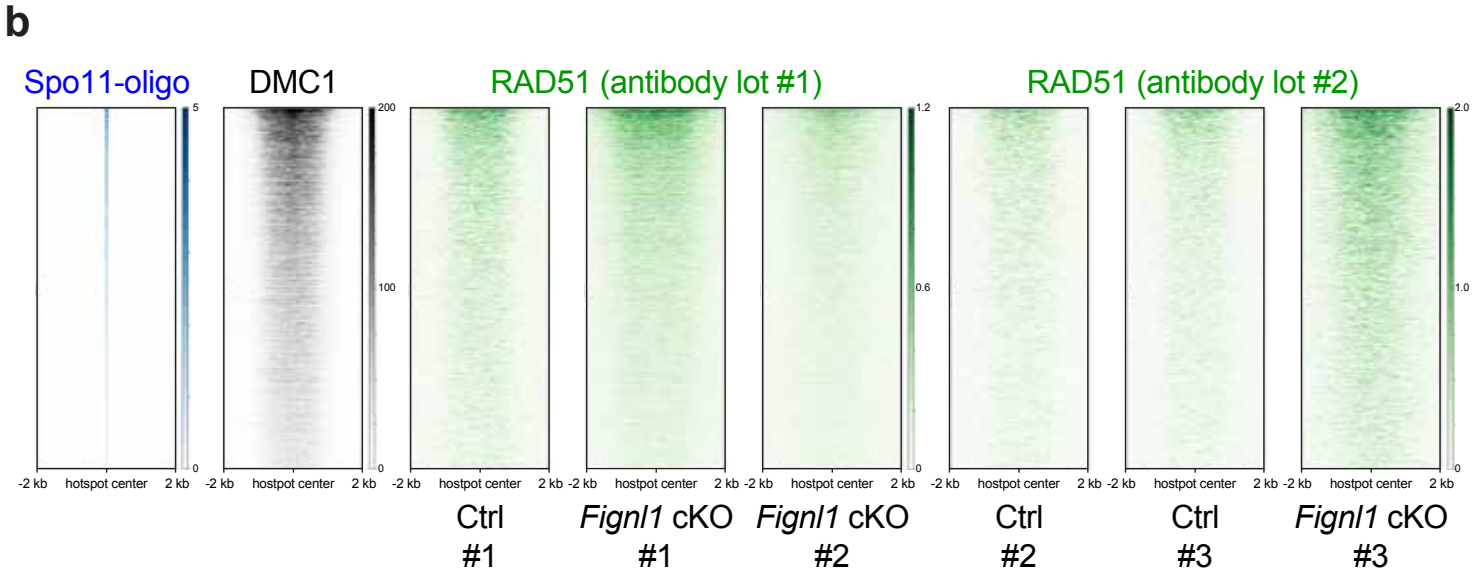


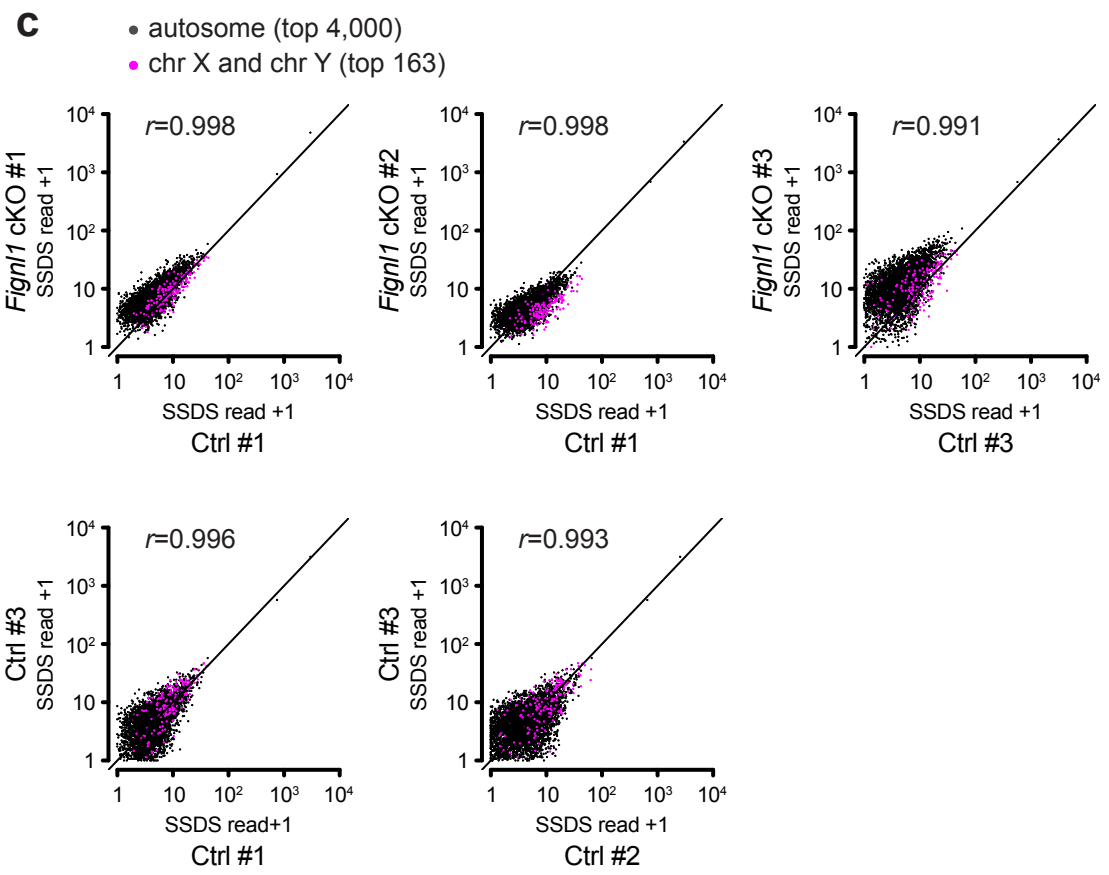


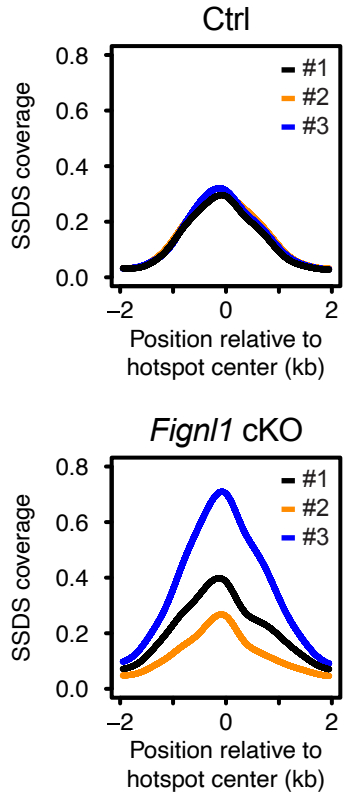

**a**

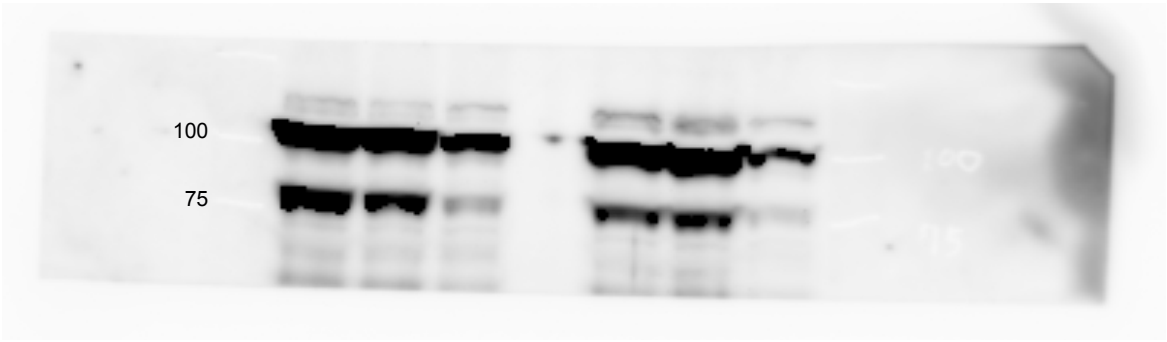


**b**

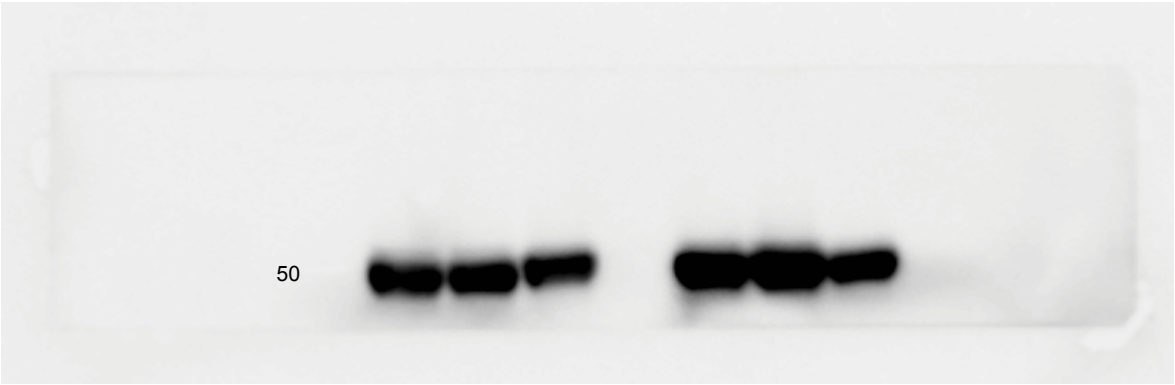


**c**

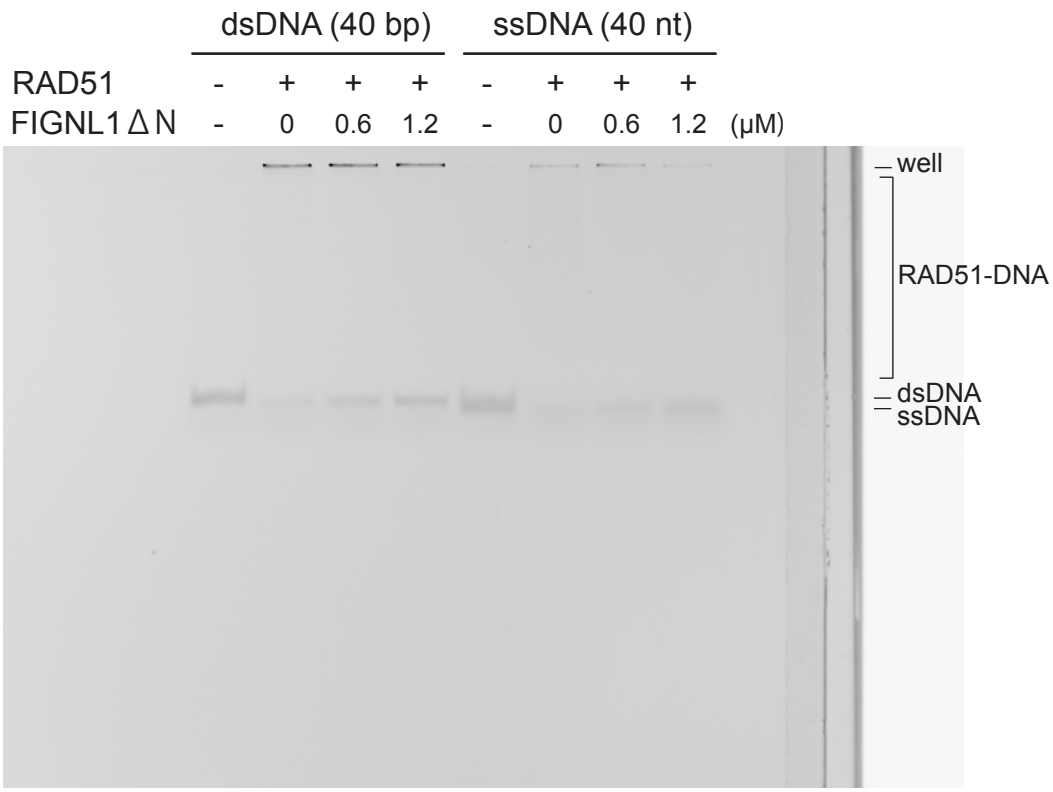


(a) An uncropped immunoblotting image for FIGNL1 shown in Fig. 1d.
(b) An uncropped immunoblotting image for α-tubulin shown in Fig. 1d.
(c) An unprocessed image of electrophoresis mobility shift assay shown in Fig. 8a.